Ga+ irradiation for zero-field skyrmion stabilization towards imaging skyrmions with SEMPA

van der Jagt, J.W.

Award date:
2019

EINDHOVEN UNIVERSITY OF TECHNOLOGY

Department of Applied Physics
Physics of Nanostructures

Ga^+ irradiation for zero-field skyrmion stabilization

Towards imaging skyrmions with SEMPA

J.W. van der Jagt

Supervisors:
dr. ir. R. Lavrijsen
M.J. Meijer MSc.

Final Version

Eindhoven, December 2019

Abstract

Skyrmions are magnetic quasi-particles with a chiral spin structure, which is of vital importance for achieving fast skyrmion velocities in future spintronic devices. In this thesis we take steps towards investigating their internal structure with scanning electron microscopy with polarization analysis (SEMPA). To achieve this, a method needs to be found to stabilize skyrmions without magnetic fields, since SEMPA is impossible in magnetic fields. We propose using an in-situ focused ion beam (FIB) to achieve zero field skyrmion stabilization in two ways. First, we can make use of the FIB to disrupt the crystal structure of a sample, changing the fundamental magnetic parameters. Second, we can use the FIB to remove material outright, which creates confining structures. An extensive set of micro-magnetic simulations is performed to investigate skyrmion stability and nucleation in confined geometries, and we show that skyrmions can indeed be stabilized in our samples at zero field. Before we are able to use the FIB in experiments, a calibration procedure is required in the form of domain wall injection experiments. We then investigate changes in the effective anisotropy and Dzyaloshinskii-Moriya interaction (DMI), as a function of the amount of intermixing caused by Ga^+ irradiation, by studying changes in domains and the internal structure of domain walls with SEMPA. We find indications of a decrease in DMI with Ga^+ irradiation and increased variations of the DMI and effective anisotropy, which is as expected for increased interface roughness after Ga^+ irradiation. The investigations into the domain walls are mostly inconclusive, but they give the first indications towards understanding how the DMI changes with Ga^+ irradiation. With the results of these experiments, we come closer to imaging skyrmions with SEMPA, since we are able to predict skyrmion stability in confining geometries and enabled the use of a FIB to tune magnetic properties.

Contents

Chapter 1

Introduction

Technical advances in the area of information processing fuel the ever growing need for fast, reliable and efficient data storage devices. Current solutions, like hard disk drives (HDDs), store information in magnetic domains, or areas with the same magnetization, on fast spinning disks. The data is accessed by a read/write head, mounted on an arm that moves over the disk. Although this is very inefficient and consumes a lot of energy, HDDs remain one of the most cost-efficient data storage methods that are currently available [1]. Data speeds can be improved, but that requires acceleration of the spinning disk and read/write head, which would cost even more energy [1]. Furthermore, the presence of moving parts make the device susceptible to failure due to mechanical wear. Faster devices without moving parts, like solid state drives (SSDs), are becoming more widespread. However, these devices have a limited amount of read/write cycles due to electron accumulation in the device. This makes them unsuitable for large data centers, where a lot of read/write cycles are happening constantly. On top of this, SSDs do not offer a significant improvement in data storage density over HDDs [2].

A solution to the above described problems was proposed by Parkin *et al.* [3] in 2008, with a new device called racetrack memory, which is visualized in figure 1.1a. Magnetic bits, with their magnetization color coded in red and blue, are stored in a strip of magnetic material. Instead of moving the magnetic strip or read/write device like in HDDs, the magnetic domains containing the information are moved by application of a current [4]. This process is significantly more efficient and does not use moving parts, eliminating physical wear as a point of failure [3]. Furthermore, this device might achieve significantly larger data storage densities comparable to HDDs, when it would be able to extend these tracks into a third dimension, as can be seen in figure 1.1a. However, racetrack memory brings with it several complications. First of all, very large current densities are required to meet the read/write speeds of current flash and SDRAM technologies [5] (roughly 10^{11} A/m^2). Second, defects in the material can hinder domain wall movement significantly, which introduces difficulties for large scale scaling [6, 7].

A potential solution to these problems can be the use of small, magnetic quasi-particles named "skyrmions". In a skyrmion, the individual magnetic moments of the electrons (spin) align in a whirling configuration. This is analogous to a 2-dimensional domain wall, defined as the region between two domains, and is shown schematically as an inset in figure 1.1b. The arrows denote the direction of the spins and are color coded from up- to down. Skyrmions have excellent properties which make them ideal candidates for many types of devices [8]. For example, the theoretical current density required to drive skyrmions through a magnetic material is low, namely 10^4 A/m^2. Furthermore, the size of skyrmions is typically on the order of nanometers [9], which reduces the effects of defects on skyrmion velocities, and their stability protects them from temperature fluctuations and magnetic fields [10, 11, 12]. Hence, using skyrmions in a skyrmionic racetrack memory [13, 14] can be an improvement on the original racetrack memory. Figure 1.1b shows the

working principles of a skyrmionic racetrack memory. The magnetic information is now encoded into the skyrmions, depicted by colored vortexes, where bits containing a skyrmion are encoded as a logical 1 and bits not containing a skyrmion are encoded as a logical 0.

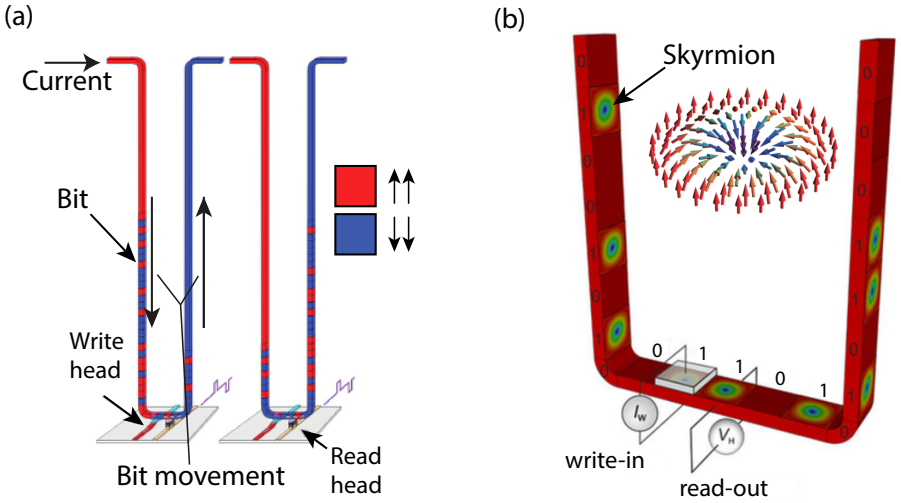

Figure 1.1: (a) Concept of racetrack memory. Magnetic domains, with the direction of the magnetization color coded in red and blue, are driven through a wire by a current along a read/write head. The direction of movement of the bits is dependent of the sign of the current. Adapted from ref [3]. (b) Skyrmionic Racetrack memory. The magnetic bits are encoded in the presence or absence of skyrmions, which can likewise be moved by application of a current. Adapted from refs [13, 15].

Before skyrmionic racetrack memory can be realized, a series of challenges needs to be overcome. The first challenge is stabilizing skyrmions without magnetic fields, which are required to stabilize skyrmions at room temperature in typical thin-film samples [8, 11], with magnetic layers only several nanometers thick. In these samples the skyrmion stability is further improved by stacking combinations of magnetic layers (e.g. Co) and heavy metal spacers (e.g. Pt or Ir) on top of each other, as shown in figure 1.2a. The layeres in the red box are typically repeated N times, before the sample is capped with a heavy metal layer. This multi-layer stacking alters sample properties by adding more magnetic material, resulting in a more robust skyrmion state [9, 11, 16, 17, 18]. However, magnetic fields are still required to stabilize skyrmions in these multi-layered samples.

The second challenge is actually forming skyrmions with the internal structure as shown in figure 1.1b in multi-layered samples, which is vital for achieving fast skyrmion velocities and consequently fast data speeds in skyrmionic devices such as racetrack memory [19]. A method that can be used to investigate the internal structure of skyrmions is scanning electron microscopy with polarization analysis (SEMPA) [20, 21, 22]. However, this technique cannot be used in magnetic fields, since the Lorentz forces from the magnetic field will disrupt the optics of the electron beam, which is used for SEMPA imaging. Hence, a method needs to be found to stabilize skyrmions at zero field before SEMPA can be used to image the internal structure of skyrmions.

In this thesis we investigate how we can stabilize skyrmions at room temperature and zero field in magnetic multi-layers, which will allow us to investigate the internal structure of skyrmions with SEMPA. We propose the use of high energy Ga^+ ion irradiation to modify the internal structures of multi-layered samples, as a method to improve skyrmion stability without application of magnetic fields. The effects of ion irradiation are shown in figure 1.2b. On the left, a typical Pt/Co/Pt multi-layered stack is shown (Co atoms in blue, Pt atoms in red). The atoms in each layer are neatly arranged. We can modify these layers by high energy Ga^+ irradiation, shown on the right in figure 1.2b. The Ga^+ ions transfer their kinetic energy to atoms in the sample, causing them

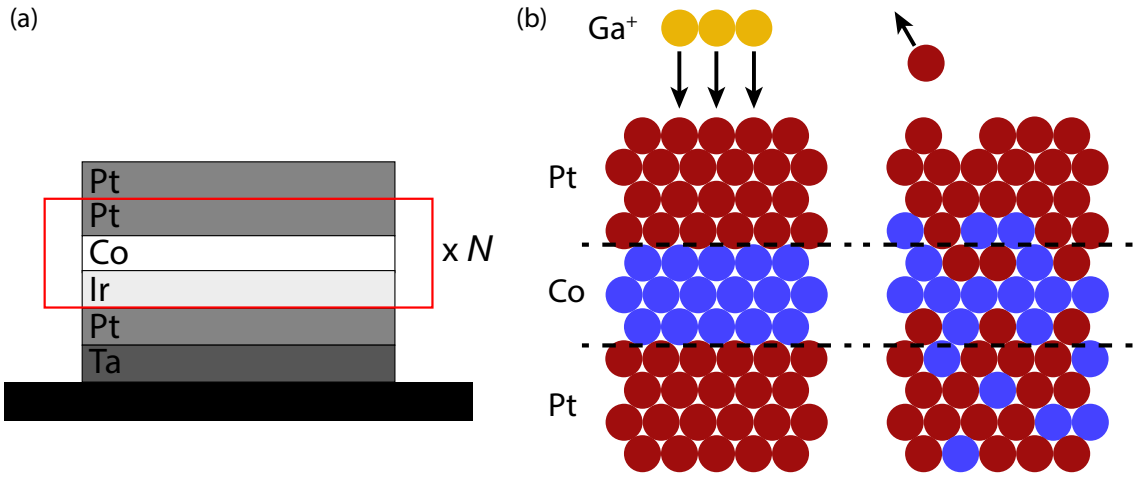

Figure 1.2: (a) Example of a typical multi-layered sample, where heavy metal layers (Pt and Ir) have been stacked on magnetic layers (Co). The layeres in the red box are repeated N times. (b) Effects of Ga^+ irradiation on a layered Pt/Co/Pt sample. On the left, the sample is schematically drawn before irradiation by Ga^+ ions. On the right, the effects are shown. The high energy Ga^+ ions can displace atoms, which will cause intermixing between layers and disrupt the interfaces between the Co and Pt layers.

to be displaced, or even ejected from the sample if their energy is large. Essentially this process is like playing billiard on an atomic scale. The interfaces between the Pt and Co layers are less well defined after Ga^+ irradiation, resulting in a change of the magnetic interactions. Hence, by ion irradiation, we can create small structures, which recent research has shown can result in stabilized zero field skyrmions at room temperature [23, 24, 25, 26], or alter the fundamental magnetic parameters, which could enhance skyrmion stabilization [27].

Specifically, in this thesis we use micro-magnetic simulations to investigate skyrmion stability and nucleation in confined geometries that would be created by Ga^+ irradiation with a focused ion beam (FIB). Before the FIB can be used in quantitative Ga^+ irradiation experiments, a calibration procedure is required. For the calibration procedure, we investigate how a domain wall is moved over an energy barrier that is dependent on the amount of Ga^+ ions coming from the FIB. By comparison with another pre-calibrated FIB, we will use these experiments to calibrate the Ga^+ fluence of the FIB that we intend to use for experiments in this thesis. In this thesis, we use qualitative Ga^+ irradiation to study how domains and domain walls change as a function of increased interface roughness caused by Ga^+ irradiation, using SEMPA.

In the next section, we will briefly summarize the goals of this thesis and describe the structure of the remainder of this thesis.

1.1 This thesis: towards imaging skyrmions with SEMPA

So far we set an ultimate goal, which is to be able to image the internal structure of skyrmions using SEMPA. To reach this goal we proposed the use of Ga^+ ion irradiation to create confined geometries and to modify magnetic parameters, which can both aid in stabilizing skyrmions at zero magnetic field, as required for SEMPA imaging. Experimentally, we can use a focused ion beam (FIB) to irradiate areas on the order of nanometers with Ga^+ ions. However, the FIB we propose to use has never been used for quantitative Ga^+ irradiation experiments before, and hence needs to be calibrated first.

To facilitate the reading of this thesis, it is structured as follows. In chapter 2, the relevant background theory and state of the art will be discussed. We will first introduce the relevant fundamental properties for the experiments in this thesis, specifically the exchange interaction, anisotropy, Zeeman effect and Dzyaloshinskii-Moryia interaction (DMI). We will focus on how they depend on interface quality, since this gives us an idea on how we can tune these parameters with Ga^+ irradiation. Furthermore, we will discuss the physics of magnetic domain walls and fundamentals of skyrmion nucleation and stabilization in confined geometries in more detail. In chapter 3, we will discuss the relevant experimental techniques and methods. Specifically we will discuss how the samples are fabricated and how a FIB can be used to modify the internal structure of the sample. Furthermore, we will discuss several imaging techniques, like SEMPA and Kerr microscopy, and we will also discuss methods for measuring the magnetic parameters of our samples. In chapter 4, we conduct an extensive set of micro-magnetic simulations to investigate the relevant parameters for skyrmion stabilization in confined geometries at zero magnetic field, as well as investigate the effects of magnetic fields on skyrmion nucleation in confined geometries. In chapter 5, we will discuss the Ga^+ dose calibration method and discuss its viability for characterizing the FIB, so that it can be used for quantitative Ga^+ dose experiments. The effects of ion irradiation on magnetic structures at nanometer scales will be investigated with SEMPA in chapter 6. Chapter 7 will contain a general conclusion of the results and an outlook for further studies and steps that need to be taken to image skyrmions with SEMPA.

Chapter 2

Theory and state of the art

The purpose of this chapter is to gain a solid understanding of the underlying theory, as well as get up to speed with the state of the art, regarding the simulations and experiments conducted in this thesis. As mentioned in chapter 1, the crux of this thesis lies in the modification of multi-layered samples with a focused ion beam (FIB). We can use a FIB to modify the interfaces between magnetic materials, which gives us control over the fundamental interactions that determine the magnetic structures (see chapter 3). In the first section, we will discuss these interactions and how we can control them with interface tuning. In the second section, we will discuss the physics of domain walls, the region in-between magnetic domains, where we focus on their behavior near energy barriers and their internal structure. In the third section, we will discuss the fundamentals of skyrmion nucleation and the effects of confinement on their stabilization.

2.1 Fundamental magnetic properties

Ferromagnets are materials, typically iron (Fe), cobalt (Co) or nickel (Ni), where the individual magnetic moments, or spins, of the electrons align in one directiondue to the Heisenberg exchange interaction. A ferromagnet can be described by the sum of the individual magnetic moments, called the magnetization $\boldsymbol{M}$. There are several other interactions that influence the direction of the magnetization. Magnetic interactions typically originate from the internal structure of a ferromagnet, applied magnetic fields and from interfaces with other materials. The full magnetization can be determined by minimizing the total energy density E_{tot} of the system. The total energy density is given by the sum of all the individual energy densities E_{i} of the relevant magnetic interactions for this thesis, given by [28]

$$E_{\mathrm{tot}} = E_{\mathrm{A}} + E_{\mathrm{K}} + E_{\mathrm{Z}} + E_{\mathrm{DMI}} + E_{\mathrm{d}}, \tag{2.1}$$

where E_{A}, E_{K}, E_{Z}, E_{DMI} and E_{d} are the energy densities for the exchange interaction, anisotropy, Zeeman effect, Dzyalonshinskii-Moryia interaction and demagnetization field, respectively (all in $\mathrm{J/m^3}$), which will be explained in the remainder of this section. We will also show how these parameters can be changed by changing the interface quality.

2.1.1 Exchange interaction

The Heisenberg exchange interaction, which is an interaction resulting from the interplay between the Pauli exclusion principle and the Coulomb interaction, favors neighboring spins to align par-

allel, as shown in figure 2.1a [28, 29].

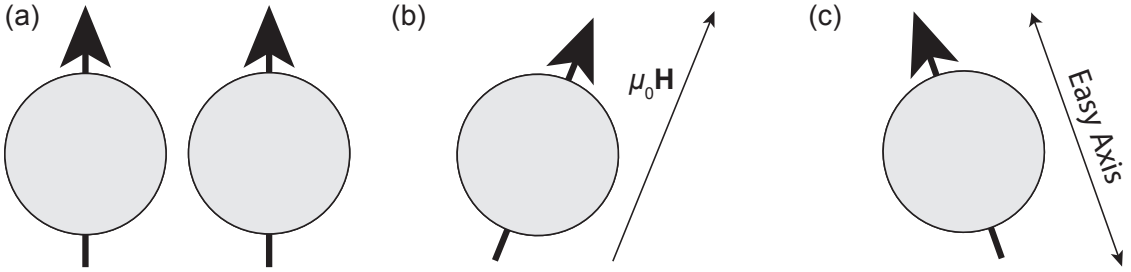

Figure 2.1: Magnetic interactions that determine the direction of the magnetization. (a) the Heisenberg exchange interaction, (b) the uniaxial anisotropy and (c) the Zeeman interaction with an applied magnetic field $\mu_0 \boldsymbol{H}$. Figure adapted from ref [30].

The energy of this exchange interaction is typically described with the Heisenberg Hamiltonian

$$H = -2J\boldsymbol{S}_i \cdot \boldsymbol{S}_j, \tag{2.2}$$

where $\boldsymbol{S}_i$ and $\boldsymbol{S}_j$ are the magnetic spins as shown in figure 2.1a and J is the exchange constant, which is positive for a ferromagnet. Expanding from two neighbouring spins to an entire lattice, all the spins in the lattice align in the same direction to form the ferromagnetic state. In this continuum limit, the corresponding exchange energy density is described by [28]

$$E_{\mathrm{A}} = A\left(\frac{\nabla \boldsymbol{M}}{M_{\mathrm{S}}}\right)^2, \tag{2.3}$$

where $\boldsymbol{M}$ is the magnetization, M_{S} the saturation magnetization (in A/m) and A the exchange stiffness (in J/m). A is related to J via [28]

$$A = \frac{S^2 Z_{\mathrm{c}}}{a} J, \tag{2.4}$$

where S is the spin, a the lattice constant and Z_{c} the amount of atoms in a unit cell. From equation 2.3 can be seen that the exchange energy is zero if $\nabla \boldsymbol{M} = 0$, i.e. when the spins are aligned parallel.

So far, it has not yet been studied how A depends on the interface quality, but since this interaction does not involve any atoms of the interfacial layers, we expect that A does not depend on interface quality, although this might be an oversimplified assumption.

2.1.2 Zeeman interactions

Applying a magnetic field $\mu_0 \boldsymbol{H}$ to a spin, as illustrated in figure 2.1b, causes the spin to align with the magnetic field [28]. This applies to all spins in the ferromagnet, which causes $\boldsymbol{M}$ to align with the magnetic field if it is strong enough to overcome all other interactions. This can be expressed in terms of the Zeeman energy, given by

$$E_{\mathrm{Z}} = -\mu_0 \boldsymbol{H} \cdot \boldsymbol{M}. \tag{2.5}$$

From equation 2.5 can be seen that the Zeeman energy is indeed minimized if the magnetization aligns with the magnetic field.

2.1.3 Anisotropy

Often the magnetization in a ferromagnet does have a preferential direction, which can be caused by the crystal structure, the shape of the ferromagnet or by interfaces of the ferromagnet with other materials. This property is called anisotropy. The simplest form of anisotropy only has one preferential direction (or easy axis). This is called uniaxial anisotropy and is visualized in figure 2.1c. The energy associated with anisotropy is described by [28]

$$E_{\mathrm{A}} = K \sin^2(\theta), \tag{2.6}$$

where θ is the angle between the magnetization and the easy axis, and K is the anisotropy constant (in $\mathrm{J/m^3}$). From equation 2.6 can be seen that the anisotropy energy is minimized if the magnetization aligns with the easy axis ($\theta = 0 \vee \pi$). As mentioned, there are several factors which give rise to the anisotropy in the thin films that are studied in this thesis. Specifically the magnetocrystalline- and shape anisotropies, which we will discuss below.

Magnetocrystalline anisotropy

For the thin film samples studied in this thesis, the magnetocrystalline anisotropy generally arises from the interfaces between the ferromagnet and other materials [31]. These materials are generally heavy metals like platinum (Pt) or iridium (Ir) with strong spin orbit coupling [32]. Due to symmetry breaking at the interface, the orbitals of the d-electrons of the ferromagnet are changed, which results in an anisotropy direction either in the plane of the sample, or along the sample normal. The latter is defined as perpendicular magnetic anisotropy (PMA) and is generally present for the thin films studied in this thesis.

The magnetocrystalline anisotropy can be separated into a volume contribution K_{v}, arising from the crystal structure and a surface contribution K_{s}, arising from the interfaces. Mathematically, this is represented as

$$K_{\mathrm{u}} = K_{\mathrm{v}} + \frac{K_{\mathrm{s,top}} + K_{\mathrm{s,bot}}}{t}, \tag{2.7}$$

where t is the thickness of the magnetic layer and $K_{\mathrm{s,top}}$ and $K_{\mathrm{s,bot}}$ the surface anisotropies of the top and bottom interfaces of the magnetic layer respectively. In the thin films studied in this thesis, the volume contribution is assumed to be negligible compared to the surface term. Hence for the rest of this thesis we assume $K_{\mathrm{v}} = 0$. The surface anisotropy is very much dependent on the quality of the interfaces between the ferromagnet and heavy metals. If the quality of the interfaces is reduced, so is the strength of the surface anisotropy [33].

Shape anisotropy

An object with uniform magnetization will have magnetic charges at each magnetic pole [34], as shown in figure 2.2 in red and blue for positive and negative charges respectively. These magnetic charges will result in a stray field outside of the object and, analogous to an electric capacitor, a magnetic field inside the object. This demagnetization field is opposite $\boldsymbol{M}$ in the object and equals $\boldsymbol{H}_{\mathrm{d}} = -\mathcal{N} \cdot \boldsymbol{M}$. Here, $\mathcal{N}$ is the demagnetization tensor, which is dependent on the shape of the object. For magnetic thin films, like the samples studied in this thesis, the demagnetization field is given by $\boldsymbol{H}_{\mathrm{d}} = -m_{\mathrm{z}}\hat{z}$ [28], where m_{z} is the z-component of the magnetization. The resulting demagnetization energy is given by

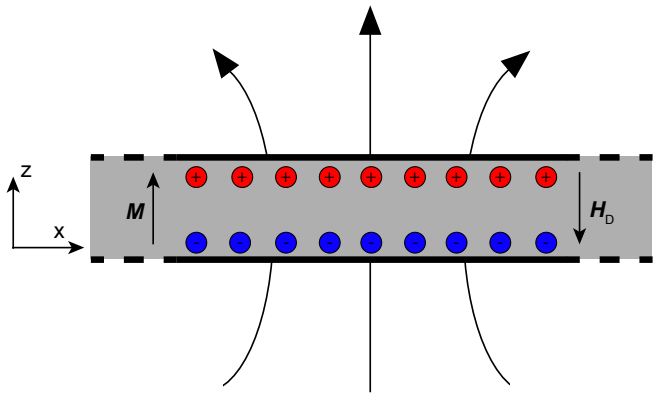

Figure 2.2: Schematic drawing showing the magnetic charges inside a uniformly magnetized thin film sample with PMA. Positive charges are shown in red and negative charges are shown in blue. The magnetization $\boldsymbol{M}$ and the resulting demagnetization field $\boldsymbol{H}_\mathrm{D}$ are depicted with arrows. Figure adapted from ref [27].

$$E_\mathrm{d} = -\frac{1}{2}\mu_0 \boldsymbol{M} \cdot \boldsymbol{H}_\mathrm{d} = \frac{1}{2}\mu_0 m_\mathrm{z}^2, \tag{2.8}$$

where μ_0 is the vacuum permeability. From equation 2.8 can be seen that if the magnetization is in-plane, the demagnetization energy is 0. Hence, due to the shape anisotropy, the most favorable orientation for the magnetization is along the plane of the thin film (in-plane). For the thin films with PMA studied in this sample, the shape anisotropy thus counteracts the magnetocrystalline anisotropy K_u and can be captured in an effective anisotropy K_eff, given by

$$K_\mathrm{eff} = \frac{K_\mathrm{s,top} + K_\mathrm{s,bot}}{t} - \frac{1}{2}\mu_0 M_\mathrm{S}^2. \tag{2.9}$$

Here the first part represents the magnetocrystalline anisotropy and the second part represents the shape anisotropy. If the magnetocrystalline anisotropy dominates, $K_\mathrm{eff} > 0$ and the magnetization will favor the out-of-plane direction. If the shape anisotropy dominates, $K_\mathrm{eff} < 0$ and the magnetization will favor the in-plane direction. From equation 2.9, we find that this balance can be tuned by varying the thickness of the magnetic layer. At large thicknesses, the surface term of the magnetocrystalline anisotropy is almost zero, resulting in a negative effective anisotropy and thus a magnetization in the in-plane direction. At small thicknesses, the surface term is strong enough such that K_eff is positive, which results in out-of-plane magnetization or PMA. For the samples in this thesis, the thickness of the magnetic layer is well below the critical thickness for the magnetization to turn in-plane [35, 36, 37] and thus the samples have positive K_eff.

2.1.4 Dzyaloshinskii-Moriya interaction (DMI)

Symmetric exchange interactions, like the Heisenberg exchange interaction, have already been discussed in section 2.1.1. They prefer parallel alignment between neighbouring spins. Antisymmetric exchange interactions, like the Dzyaloshinskii-Moriya interaction (DMI) [38, 39], instead favor perpendicular alignment between neighbouring spins. Coming back to a description of two spins, the energy associated with the DMI is captured in the Hamiltonian [12]

$$H_\mathrm{DMI} = -\boldsymbol{D}_{ij} \cdot (\boldsymbol{S}_i \times \boldsymbol{S}_j), \tag{2.10}$$

where $\boldsymbol{D}_{ij}$ is the DMI vector between the two spins $\boldsymbol{S}_i$ and $\boldsymbol{S}_j$. The working principles of the DMI are schematically represented in figure 2.3. Here it can be seen that the DMI is mediated through a heavy metal atom, shown in blue, with strong spin orbit coupling [40]. This results in a canting of spins in the ferromagnet, shown with red atoms. Due to symmetries, the DMI vector is purely in the y-direction. Depending on the sign of D, the canting direction of the spins in the ferromagnet is inwards instead of outwards. Note that the DMI is only present when the symmetry at the interfaces is broken, which is the case for the thin film samples used in this thesis. In figure 2.3, the symmetry is broken at the interface between the heavy metal and the ferromagnet. If we put the same heavy metal layer on top, the symmetry is broken again. In these symmetric stacks, like Pt/Co/Pt, the DMI resulting from the symmetry breaking at both interfaces has an opposite sign and hence is canceled out. Putting a different heavy metal layer at each interface, like in asymmetric stacks such as Ir/Co(B)/Pt, can result in a DMI where the magnitude of the DMI at each interface can be different, and / or the sign of the DMI at each interface can be the same. This results in a net DMI. Both symmetric and asymmetric stacks will be used in this thesis.

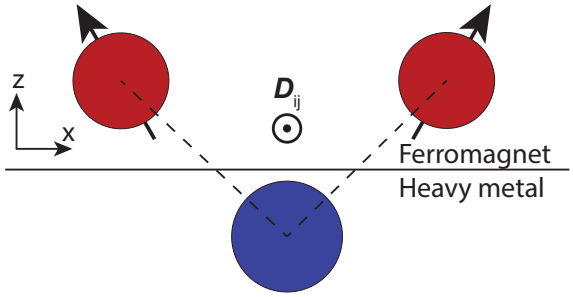

Figure 2.3: Schematic overview of the principles of the Dzyaloshinskii-Moriya interaction at the interface between a ferromagnet (red) and a heavy metal (blue) layer.

The energy associated with the DMI for the thin films studied in this thesis is given by [41]

$$E_{\mathrm{DMI}} = \frac{D}{M_{\mathrm{S}}^2} \left(m_{\mathrm{z}} \left(\nabla \cdot \boldsymbol{M} \right) - \left(\boldsymbol{M} \cdot \nabla \right) m_{\mathrm{z}} \right), \tag{2.11}$$

where D is the magnitude of the DMI vector. When it is assumed that canting of the magnetization is only present in the x-direction, as shown in figure 2.3, we can see from equation 2.11 that if $\boldsymbol{M}$ reverses sign in the x-direction, which is effectively changing the direction of the canting, the entire DMI energy changes sign. Thus, only a specific canting direction, inwards or outwards is stabilized, depending on the sign of D.

The DMI as described here originates from the interface and is therefore dependent on the thickness of the magnetic layer t via $D = \frac{D_{\mathrm{s}}}{t}$, where D_{s} is the surface DMI constant. By changing the thickness of the magnetic layer, the DMI can thus be changed. Much like the surface anisotropy K_{s} (see section 2.1.3), D_{s} is very much dependent on the interface quality. If the interface roughness is large, the symmetry considerations that resulted in a $\boldsymbol{D}$ purely in the y-direction are not valid anymore. Hence, individual $\boldsymbol{D}_{ij}$ have a larger spread in directions, which results in a lower average D_{s}. Franken *et al.* reported that D_{s} can be varied by tuning the thickness of a the heavy metal layer at the interface with the magnetic layer [42], which highlights the importance of the interface characteristics on the DMI strength.

2.1.5 Domain formation

Taking into account all the interactions described so far in this section, typical samples with PMA have a magnetization as depicted in figure 2.4a. As adressed in section 2.1.3, magnetic charges

are present at each magnetic pole, resulting in a demagnetization field inside the sample and stray fields outside the sample. Maintaining these stray fields costs energy. Stray fields (depicted by black arrows) leak into the surrounding environment, resulting in a very high demagnetization field and thus energy. To reduce this energy, a region with magnetization that is anti-parallel can be formed, as is visualized in figure 2.4b. The red and blue areas represent the up- and down domains respectively, with a white arrow denoting the direction of the magnetization. The stray fields from these regions combine, which reduces the amount of magnetic flux that leaks into the environment. Hence, the demagnetization energy is reduced [28].

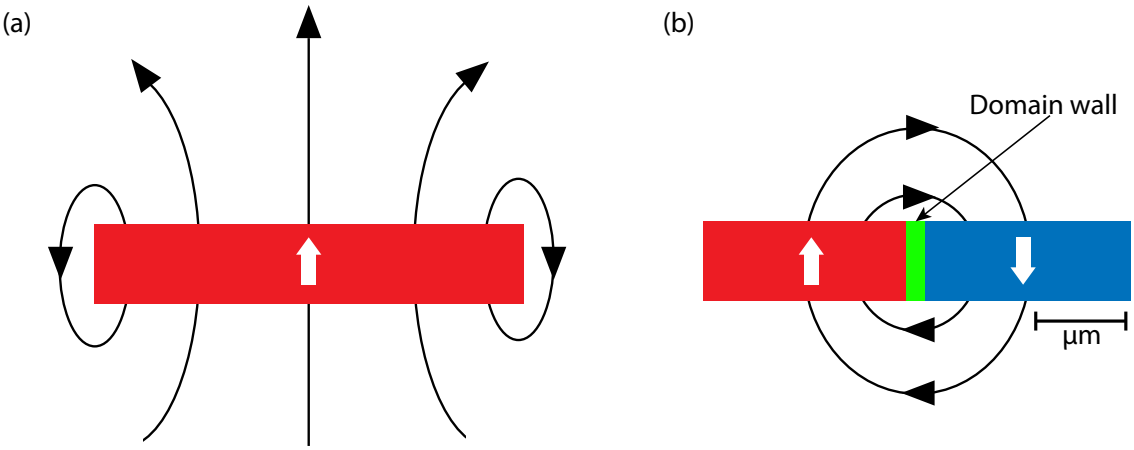

Figure 2.4: Schematic drawing of the stray fields of a magnetic layer with (a) uniform magnetization and (b) a multi-domain state. The black arrows denote the magnetic stray fields. An up-domain is represented in red, and a down domain is represented in blue. The white arrows denote the direction of the magnetization.

The region with opposite magnetization is energetically equivalent to the original region in samples with PMA, hence no energy penalty is paid to reverse the magnetization. These regions where the magnetization is uniform is called a magnetic domain. Minimization of the demagnetization energy favors the creation of many domains, commonly referred to as a multi-domain state. Although opposite domains are energetically equivalent, intermediate regions are formed, called domain walls as depicted in green in figure 2.4b. The energy associated with the formation of domain walls will be discussed in the next section. The formation of domains is thus dependent on the relative strengths of the demagnetization energy and the domain wall energy. A domain is formed if the demagnetization energy is larger than the domain wall energy.

2.2 Domain walls

In this section we will discuss the regions in between magnetic domains, called domain walls. We will start with a discussion on the basic physics of domain walls. Once a solid foundation is laid, we will treat a model for the domain wall chirality, defined as the rotational direction of the magnetization in the domain wall.

2.2.1 Fundamentals of domain walls

As mentioned in section 2.1.5, the formation of a domain wall costs energy. The surface energy density of a domain wall, defined as the energy penalty that needs to be paid to form a domain wall, is given by [43]

$$\sigma_{\mathrm{DW}} = 4\sqrt{AK_{\mathrm{eff}}} - \pi|D|, \tag{2.12}$$

where σ_{DW} is the domain wall surface energy density in J/m^2 and $|D|$ is the magnitude of the DMI vector in J/m^2. The first part of equation 2.12 is the energy of a domain wall without DMI. It is positive, since A favors parallel alignment between neighboring spins and K_{eff} favors alignment of the spins with the easy-axis, in this case up- or down. Hence, to form a rotating spin structure like a domain wall, an exchange and anisotropy energy penalty has to be paid. The second part of equation 2.12 is added in systems that have DMI. As mentioned in section 2.1.4, the DMI favors rotation between neighboring spins. Hence, the DMI is favorable for domain wall formation and lowers the domain wall surface energy density. The total domain wall energy can be calculated by integrating over the total length of the domain wall and multiplying by the thickness of the magnetic layer.

The width of a domain wall Δ is given by [28, 44, 45]

$$\Delta = \sqrt{\frac{A}{K_{\mathrm{eff}}}}. \tag{2.13}$$

Δ is thus dependent on the balance between the exchange interaction and the effective anisotropy. Exchange interactions favor switching from up- to down magnetization over long distances to minimize the angles between neighboring spins, which causes large domain widths, as can be seen in equation 2.13. Conversely, the effective anisotropy favors fast switching to reduce the amount of spins that are misaligned with the easy axis (normal to the surface in the case of the thin films studied in this thesis). Typical samples that are studied in this thesis have an exchange coupling on the order of 10 pJ/m and an effective anisotropy between 0.1 and 1 MJ/m^3, resulting in typical domain wall widths between 10 and 100 nm.

There are two types of domain walls in the typical thin film samples studied in this thesis; Bloch and Néel domain walls, which are depicted in figures 2.5a and 2.5b respectively. The red areas and blue areas denote the domains with up- and down magnetization respectively, while the green areas denote the domain walls. The magnetization in the Bloch domain wall rotates in the y-direction, or tangential planes, while the magnetization in the Néel wall rotates in the x-direction, or in the plane of the domain wall. Which type of domain wall is favored in the sample depends on the geometry of the sample [46] and, as will be discussed in more detail in section 2.2.2, interplay between the DMI and dipolar interactions. Generally for thin films the DMI favors Néel walls with rotation in the x-direction, as can be seen from equation 2.11. The interplay between the DMI and the dipolar interaction does not just determine which domain walls are favored, it also allows us to determine the direction of rotation in a Néel wall, defined as its chirality. This is discussed in more detail in section 2.2.2. When the DMI is absent Bloch walls are favored, since they do not have a net magnetization in the x-direction, which reduces the stray field energy of the domain wall.

In section 2.1.5 we mentioned that the formation of domains and domain walls arises on the interplay between the domain wall energy and the demagnetization energy, with the sizes of the magnetic domains dependent on the relative strengths of these interactions [47]. In chapter 6 we will tune the interplay between these parameters by tuning the interface quality with Ga^+ irradiation. From this we could possibly extract changes in the DMI from the changes in domain width due to Ga^+ irradiation. Furthermore, we will tune the width of domain walls to possibly extract changes in K_{eff} due to Ga^+ irradiation.

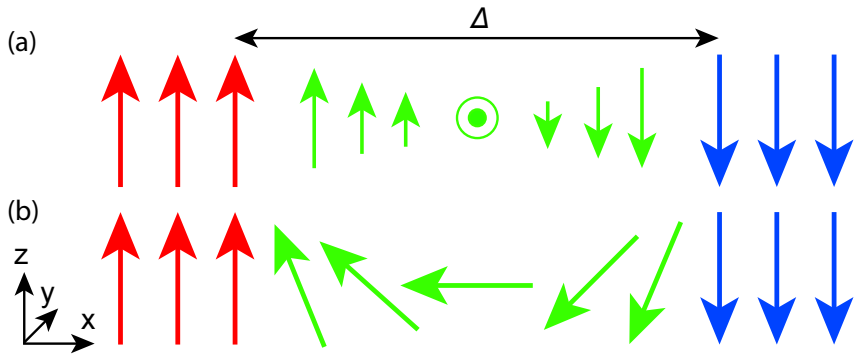

Figure 2.5: Two types of domain wall configurations. In red and blue, the up- and down- domains are shown, with the domain wall indicated in green for (a) a Bloch domain walls and (b) a Néel domain wall. The domain wall width is indicated by Δ.

2.2.2 Domain walls in multi-layered samples

Until now we looked at the formation of domain walls in single magnetic layers. In the experiments in this thesis, samples with multiple magnetic layers and heavy metal spacer layers are used. In this section, we will describe how domain walls change in these kinds of multi-layered samples. Particularly, we will focus on the rotational direction of the magnetization in the domain walls between up- and down domains, defined as the chirality. We will see that the domain wall chirality is dependent on the interplay between the DMI and dipolar energy. This is described in detail in a model by ref [48], which we will use to describe the physics of domain wall chirality in this section. In chapter 6, we will use Ga^+ irradiation to tune the balance between the DMI and dipolar energies. From this we could be able to extract the changes in DMI, by looking at the changes in domain wall chirality due to Ga^+ irradiation.

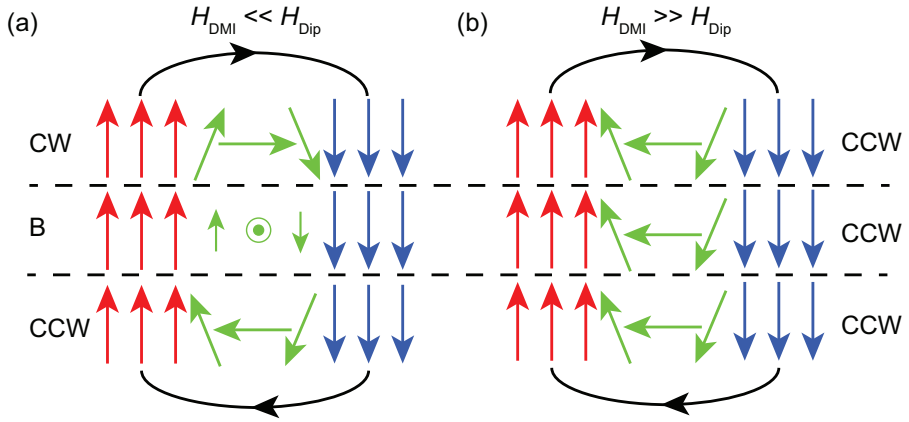

Figure 2.6: Nanoscale magnetic structure of a domain wall (green) in a multi-layered system with 3 magnetic layers (up domains in red, down domains in blue), separated by dashed lines. The black lines denote the direction of the stray fields coming from the sample. (a) In this system the dipolar energy dominates ($H_{\mathrm{DMI}} \ll H_{\mathrm{dip}}$). Néel caps are formed due to alignment with the stray fields. (b) In this system the DMI energy is dominant ($H_{\mathrm{DMI}} \gg H_{\mathrm{dip}}$). The domain walls are all of the same chirality due to the DMI. Figure adapted from ref [49].

Domain wall chirality is influenced by several parameters. Recently it was found that the dipolar energy can stabilize chiral domain walls [48]. This effect is shown in figure 2.6a. The stray fields coming from the magnetic domains (red and blue) align the domain walls (green) to form

clockwise (CW) and counter-clockwise (CCW) Néel walls in the top and bottom layers respectively, also referred to as Néel caps [44, 50]. In the centre there is no alignment with the stray fields and hence a Bloch (B) wall is the most favorable configuration. In single-layered samples, the strength of the dipolar energy is too small to influence the chirality. However in multi-layered samples, the effect of the dipolar energy on the domain wall chirality has to be taken into account, due to the added magnetic volume from multi-layer stacking [48]. The dipolar energy is not the only interaction that can stabilize a domain wall. As mentioned in section 2.1.4, the DMI favors an angle between neighbouring spins, which is beneficial for stabilizing a specific domain wall chirality [19, 48, 51, 52, 53, 54]. This effect is shown in figure 2.6b. The chirality of the domain walls is the same in every layer due to the large DMI, in this case CCW. In the top layer, the domain wall is misaligned with the stray fields, which results in an energy penalty. The competition between the dipolar energy and DMI stands at the basis of the model in ref [48].

The competition between the dipolar energy and the DMI is schematically shown in figure 2.7. A magnetic layer (CoB in this case), is depicted on top of a multi-layered stack, separated by a spacer layer. The effective fields of the DMI and dipolar energies are indicated with pink and black arrows respectively. Depending on the relative size of the effective fields, the chirality of the domain wall in the top layer will either be CW or CCW [48]. Since in this case the DMI is dominant, a CCW Néel wall is formed, as indicated in green in figure 2.7.

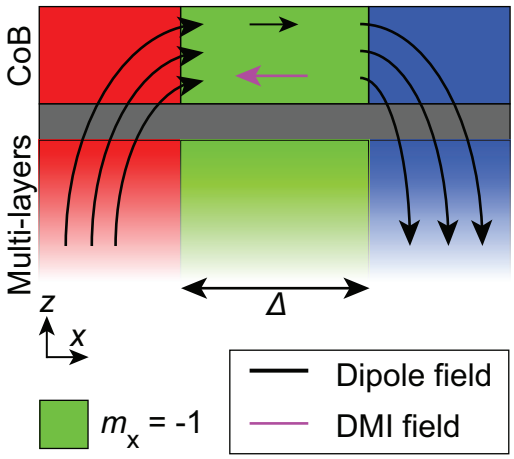

Figure 2.7: Schematic drawing of the basics of the model from ref [48]. A CoB layer on top of a multi-layered stack, separated by a spacer layer, with a CCW Néel wall indicated in green. The two effective in-plane fields for the DMI and dipolar interactions are indicated with pink and black arrows. Δ denotes the domain wall width. Figure adapted from ref [37].

As mentioned in refs [19, 51, 52], the interplay between the DMI and dipolar energies is also of vital importance in the stabilization of skyrmions, whose physics will be discussed in the next section.

2.3 Skyrmions

Skyrmions are magnetic quasi-particles with a chiral internal spin structure, which is visualized in figure 2.8. The arrows denote the spin of the electrons in the skyrmion and are color coded to the up (red) or down (blue) direction. A Bloch type skyrmion is shown in figure 2.8a where, like the Bloch domain wall, the magnetization rotates from up to down in tangential planes perpendicular to the skyrmion radius. From the cross section, which is shown below the Bloch skyrmion, we indeed see that the skyrmion consists of a Bloch domain wall, continuously rotated along 360°.

Néel type skyrmions, which are shown in figure 2.8b, have magnetization rotating in the radial direction, and are likewise made up of a 360° Néel domain wall.

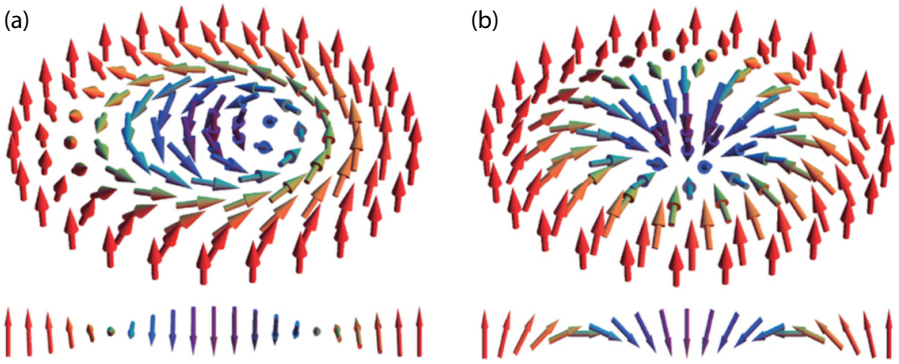

Figure 2.8: Schematic representations of a skyrmion. (a) A skyrmion in the Bloch configuration. (b) A skyrmion in the Néel configuration. A cross section of the skyrmion is shown below each skyrmion type. Figure from [15].

In this section, we will discuss the interactions involved with the nucleation and stabilization of skyrmions. First in thin films (section 2.3.1) and later also in confined geometries (section 2.3.2), the latter of which will be used for the simulations in chapter 4.

2.3.1 Skyrmion energy fundamentals

Since a skyrmion can be seen as a continuously rotated 360° domain wall, we can use the physics of domain walls, as discussed in section 2.2, as a starting point to discuss how skyrmions are created and stabilized. Hence, the domain wall surface energy density σ_{DW} can also be used to describe skyrmion energies. Since D is such a vital parameter in the stabilization of chiral structures, we will express the sign of σ_{DW} with a critical value of the DMI, since D lowers σ_{DW}. This critical value is given by

$$D_{\mathrm{crit}} = \frac{4}{\pi}\sqrt{AK_{\mathrm{eff}}}. \tag{2.14}$$

For $D > D_{\mathrm{crit}}$, σ_{DW} is negative, meaning the system wants to form as many domain walls as possible, creating a spin spiral state (see ref [11]). For the typical samples used in this thesis, $D < D_{\mathrm{crit}}$ and thus σ_{DW} is positive, where the formation of a domain wall costs energy and thus a multi-domain state is formed [8], as can be seen in figure 2.9a. The up and down domains are respresented by yellow and blue colors respectively. Application of a magnetic field will cause the domains aligned with the magnetic field to grow and the domains anti-parallel with the magnetic field to shrink, which increases its Zeeman energy. At this point skyrmions can be formed in the sample to retain some DMI energy, as shown by the yellow dots in figure 2.9b. Here the skyrmions have a larger inner area than as depicted in figure 2.8. The gain in DMI energy is not large enough to warrant the formation of a full skyrmion lattice, and instead only individual skyrmions are present [8].

In general, an applied magnetic field is needed to nucleate a skyrmion (lattice). However, as explained in chapter 1, the SEMPA technique does not work in magnetic fields. Hence, another method of stabilizing skyrmions needs to be investigated. In this thesis, we use of confined structures, whose effects on skyrmion stabilization are explained in the next section.

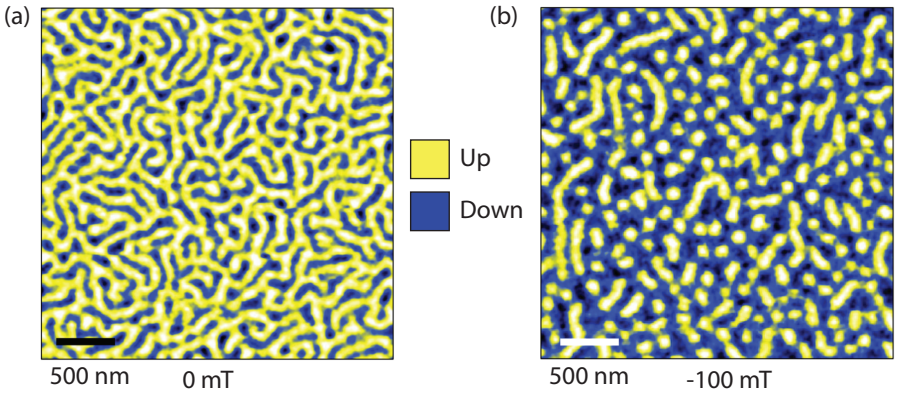

Figure 2.9: Magnetic force microscopy images of a Pt/Co/Fe/Ir multi-layered stack (a) at zero field. A multi-domain state is present, with the up and down domains represented by yellow and blue colors respectively. (b) Image at an applied field of -100 mT. Isolated skyrmions, represented by the yellow dots, appear in-between the multi-domain state. The skyrmions have a larger inner area than as depicted in figure 2.8. Both figures from ref [18].

2.3.2 Skyrmions in confined geometries

So far we have described the energies involved in the nucleation of a skyrmion in full sheet samples without constraining boundary conditions. As mentioned in section 2.3.1, a magnetic field is required for skyrmion stabilization. However in this thesis, we aim to use confined geometries to stabilize skyrmions at zero field. Hence, we have to take into account the role of confinement on the stabilization of skyrmions, which is studied in more detail in chapter 4.

The effect of confinement on skyrmion stability can be explained in a simple picture as follows [55]. Confined structures introduce edge effects, which can be ignored in full sheet samples. Specifically, the DMI at the edge of a magnetic structure causes the magnetization to tilt, since that minimizes the total energy, as shown by Rohart and Thiaville [23]. The tilted magnetization is fixed, which limits the position and expansion of skyrmions. This is shown with a cross-sectional overview in figure 2.10. In figure 2.10a, the cross-section of a skyrmion in a nanodot is schematically shown. The skyrmion profile is shown in blue, with the surrounding magnetization in red. The magnetization at the edges, which is shown in grey, is tilted and fixed due to the DMI.

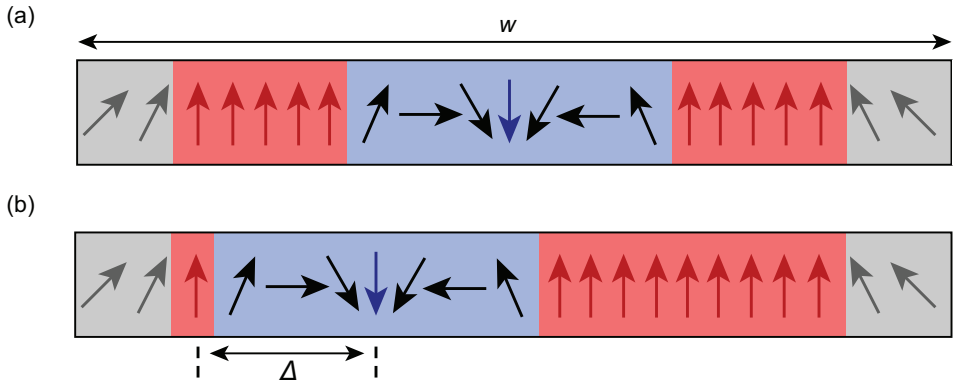

Figure 2.10: (a) Cross-section of a skyrmion in a nanodot with width w. The skyrmion is indicated in blue, the red areas denote the surrounding magnetization and the grey areas denote the fixed tilted magnetization at the edges of the nanodot due to the DMI. Δ denotes the domain wall width. (b) Skyrmion at the edge of a nanodot. Figure adapted from ref [55].

In figure 2.10b, the skyrmion is shifted towards the left. If the skyrmion is moved even further, its spin structure will be compressed, which increases the domain wall energy. Hence, an effective repelling force acts on the skyrmion and the edge, resulting in a limited position of the skyrmion. This force confines the skyrmion in the nanodot. The effective distance of this force is on the same scale as the domain wall width Δ, which is on the order of 30 nm for the typical samples in this thesis. In chapter 4, we use structures that are typically 100 - 1000 nm in diameter, which makes this repelling effect due to DMI an important interaction for the stabilization of skyrmions in confined structures, according to ref [56]. At larger diameters, dipolar interactions become significant enough for stabilizing larger skyrmion bubbles, as shown by ref [57], however this effect is only significant on the micrometer scale. Hence the main factor for skyrmion stabilization in the nanodots used in this thesis is the repelling force from the spin tilting at the edges due to the DMI.

2.4 Summary

To recap, in this chapter we have described the background physics and state of the art required to understand the experiments and results in this thesis. We have described the exchange stiffness, effective anisotropy, Zeeman effect and the Dzyaloshinskii-Moriya interaction (DMI), and how they depend on interface quality, since this can be tuned with Ga^+ irradiation. Specifically, we expect A and M_S to be invariant with Ga^+ irradiation and K_{eff} and D to decrease with Ga^+ irradiation. Next we discussed the formation of domains and domain walls, resulting from the balance between the demagnetization energy and domain wall energy. We further elaborated on the size and internal magnetization profile of domain walls in multi-layered systems, with the latter defined as the chirality, and how the chirality is determined by the interplay between the DMI and dipolar energies. We expect clockwise chirality for a dominant dipolar energy and counter-clockwise chirality for a dominant DMI. We have also discussed the nucleation of skyrmions and the effects of confinement on their stabilization. In the next chapter, the experimental techniques used in the experiments in this thesis will be discussed.

Chapter 3

Experimental methods and techniques

In this chapter, the experimental techniques and methods used for the simulations and experiments of this thesis will be discussed. We will start by discussing the sample fabrication techniques, specifically magnetron sputtering and electron beam lithography (EBL), and the samples used in this thesis. Afterwards, we will discuss how we can manipulate these samples with a focused ion beam (FIB), which can be used to manipulate the interfaces of magnetic multi-layered samples. This gives us control over several interface dependent magnetic properties. Next we will briefly introduce the basics of the micro-magnetic simulations used in chapter 4 of this thesis, where we will investigate the stability of skyrmions in confined geometries. Finally, we will discuss the techniques we used to characterize the samples in this thesis. We used Kerr microscopy to image domains, SEMPA to image domains and domain walls on the nanometer scale and SQUID-VSM to determine M_S and K_{eff}.

3.1 Sample Fabrication Techniques

3.1.1 Magnetron sputtering

The samples used in this thesis are fabricated by magnetron sputtering. With this method, we can create material layers with a thickness in the order of nanometers. This technique is schematically shown in figure 3.1. During the process, a steady flow of argon (Ar) gas is pumped through the chamber, typically at pressures of roughly 10^{-2} mbar. The sputtering chamber is kept at a pressure of roughly 10^{-9} mbar when no material is being deposited. By applying a large potential between the chamber and the target, which contains the desired deposition material, an Ar plasma is created. High energy Ar^+ ions collide with the target, which dislocate atoms from the target, indicated in the right image in figure 3.1. These atoms are subsequently deposited on the substrate, eventually growing a layer of material. The growth rate is dependent on the Ar pressure and applied voltage the distance between the target and the substrate, and is typically on the order of 1 Å/s [58]. By linearly moving a shutter over the substrate during the growth process, the thickness of the layer can be varied spatially. This allows for thickness dependent studies. Hence, magnetron sputtering is a very versatile technique for sample fabrication.

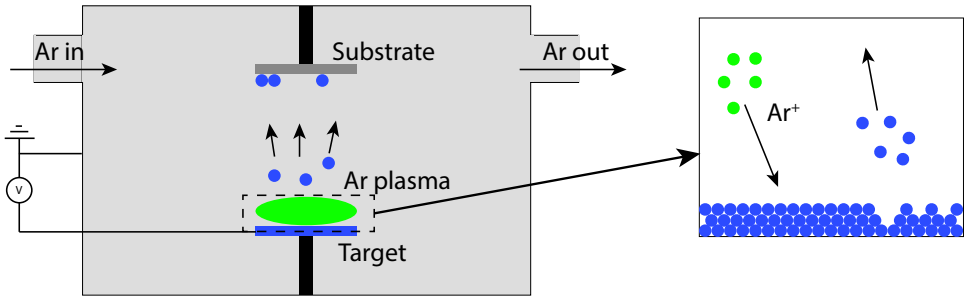

Figure 3.1: Schematic representation of the magnetron sputtering process. High energy particles (green) from an argon plasma remove atoms from a target material (blue). These atoms are then deposited on the substrate. Figure adapted from ref [27].

3.1.2 Sample details

In this thesis, we study three different samples, which are shown in figure 3.2. All these samples were grown with the magnetron sputtering technique, described in section 3.1.1. In this section, we will discuss the sample characteristics and discuss the motivation behind investigating these samples. For all samples, the thickness of each layer is indicated between parentheses in nanometers.

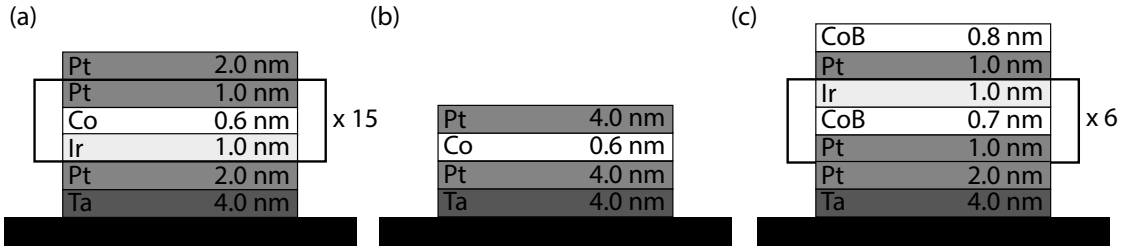

Figure 3.2: Schematic overview of the samples used in this thesis. (a) Ta(4)/Pt(2)/$[\text{Ir}(1)/\text{Co}(0.6)/\text{Pt}(1)]_{\text{x15}}$/Pt(2), used in chapter 4, (b) Ta(4)/Pt(4)/Co(0.6)/Pt(4), used in chapter 5 and (c) Ta(4)/Pt(2)/$[\text{Pt}(1)/\text{Co}_{80}\text{B}_{20}(0.7)/\text{Ir}(1)]_{\text{x6}}$/Pt(1)/$\text{Co}_{80}\text{B}_{20}(0.8)$, used in chapter 6. For all samples, the thicknesses are indicated in nanometers.

All three samples use a Si substrate with a thermally oxidized SiO_2 layer of roughly 100 nm, and a tantalum (Ta) seed layer of 4 nm, to aid the growth of the platinum (Pt) layers. The magnetic layers are either cobalt (Co) or cobalt-boron ($Co_{80}B_{20}$), with the latter of the two having a lower M_S and K_{eff}. The heavy metals are either Pt or iridium (Ir), stacked symmetrically or asymmetrically to eliminate or enhance the DMI.

For the micromagnetic simulations in chapter 4, we study skyrmions in cylindrical nanodots consisting of Ta(4)/Pt(2)/$[\text{Ir}(1)/\text{Co}(0.6)/\text{Pt}(1)]_{\text{x15}}$/Pt(2), shown in figure 3.2a. We study this particular sample, since experiments have already been conducted with it [59]. Hence, we can use the simulation results to verify the experimental results. Furthermore, since the sample was already characterized by ref [27], we can use their values for M_S and K_{eff} in the simulations. Specifically for the sample, Ir and Pt are to create a large DMI in the sample and Co is chosen such that the sample is in an as-deposited multi-domain state. This stack is repeated 15 times to increase the magnetic volume and thus the strength of the dipolar interactions, while keeping the interface interactions constant. The addition of this magnetic volume is vital for room temperature stability of skyrmions [16].

In chapter 5, we use Ta(4)/Pt(4)/Co(0.6)/Pt(4) wires for domain wall injection measurements

to calibrate the in-situ FIB. This sample is shown in figure 3.2b. The domain wall injection experiment is based on work by ref [60], hence we elect to use a similar sample. Furthermore, a Co thickness of 0.6 nm was chosen, since it retains its PMA for a larger Ga^+ dose than samples with a thinner Co layer [60].

In chapter 6, we conduct SEMPA measurements (see section 3.4.2) on a multi-layer stack of $Ta(4)/Pt(2)/[Pt(1)/Co_{80}B_{20}(0.7)/Ir(1)]_{x6}/Pt(1)/Co_{80}B_{20}(0.8)$. This sample is shown in figure 3.2c. In this sample, we used CoB instead of Co because of its lower M_S and K_{eff}, which were required to form the as-deposited multi-domain state we need to investigate the domain structure. Here we again used Pt and Ir for their large and additive DMI. Furthermore, we repeated this stack 6 times to increase the magnetic volume and thus the strength of the dipolar interactions. This sample has already been studied in ref [37] and hence we can use results from ref [37] in our experiments.

3.1.3 Electron beam lithography (EBL)

Lithographic techniques are generally used to create very small and precise structures. The experiments in chapter 5 use 1×10 μm^2 wires, which are created using the EBL technique. The EBL technique is schematically drawn in figure 3.3. First, we cover the substrate with a polymeric material, often a form of polymethylmethacrylate (PMMA). The 950K and 495K layers indicate the length of the polymer chains. Then, we expose areas of the PMMA to a beam of high energy electrons of roughly 30 keV. This causes the bonds between the polymers to break, making it easier to dissolve. In step 2, we develop the sample by dissolving the exposed areas in a methylisobutylketon (MIBK) and isopropylalcohol (IPA) mixture. The sample spends just the right amount of time in this mixture to only dissolve the exposed areas. In step 3, we cover our sample with the desired metal layers (ML) by magnetron sputtering (see section 3.1.2). At the exposed areas the material attaches to the substrate, while at the unexposed areas the material is put on top of the PMMA layer. The last step is the lift-off step, where the remaining PMMA is dissolved in acetone. This removes all the unwanted materials grown on top of the PMMA layers and leaves only the desired structures on the substrate.

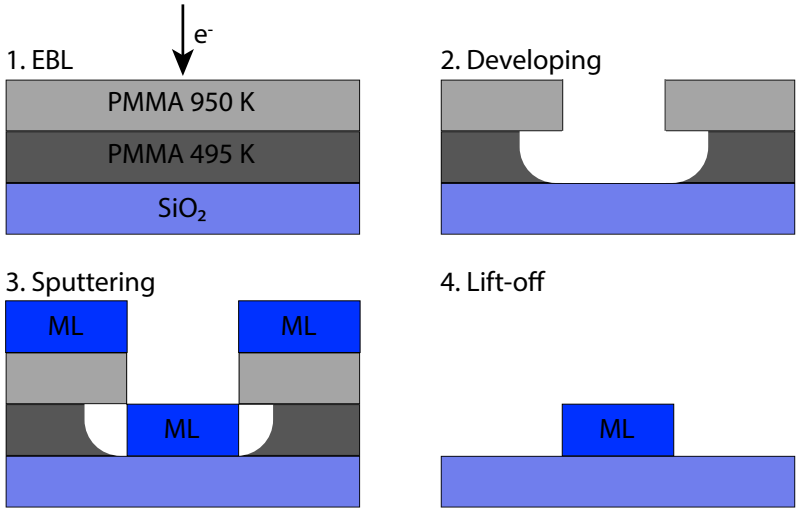

Figure 3.3: Schematic drawing of the 4 steps used in EBL. The sample is covered in PMMA. It is then exposed to an electron beam, which destroys the PMMA. By developing, certain areas of the sample are freed from PMMA. By then sputtering a metal layer (ML) on top of the sample and removing excess PMMA with acetone, only the desired structures remain. Adapted from ref [61].

3.2 Focused Ion Beam

Over the last years, the focused ion beam (FIB) has increasingly been used in material studies and technological applications due to its high-resolution imaging capabilities and capabilities of modifying the sample structure on the nanometer scale [62, 63, 64, 65, 66]. Among other uses, a FIB can be used to displace atoms in the sample, disrupting the crystal structure and giving us control over the fundamental magnetic parameters resulting from the crystal structure or interfaces with other materials. In this section, we will first introduce the working principles and optics of a focused ion beam. After this has been treated, we will discuss the interactions between high energy ions and the sample in more detail, specifically on the interfaces between the materials.

3.2.1 FIB optics and working principles

A reliable source of high energy ions is needed to use the FIB. The typical ion source that is used for a FIB is the liquid metal ion source (LMIS). A schematic drawing of a LMIS is shown in figure 3.4a. A thin layer of liquid metal, commonly gallium (Ga), surrounds a tungsten (W) rod. Due to gravity, the liquid metal will be dragged down and, as a result of the balance between adhesive forces and gravity, take on a cone shape, called the Taylor cone [62]. By applying a large potential between the LMIS and an extraction electrode (indicated in green), usually on the order of 10 kV, ions can be extracted from the Taylor cone. The energy of the ions depends on the applied potential to the LMIS [62].

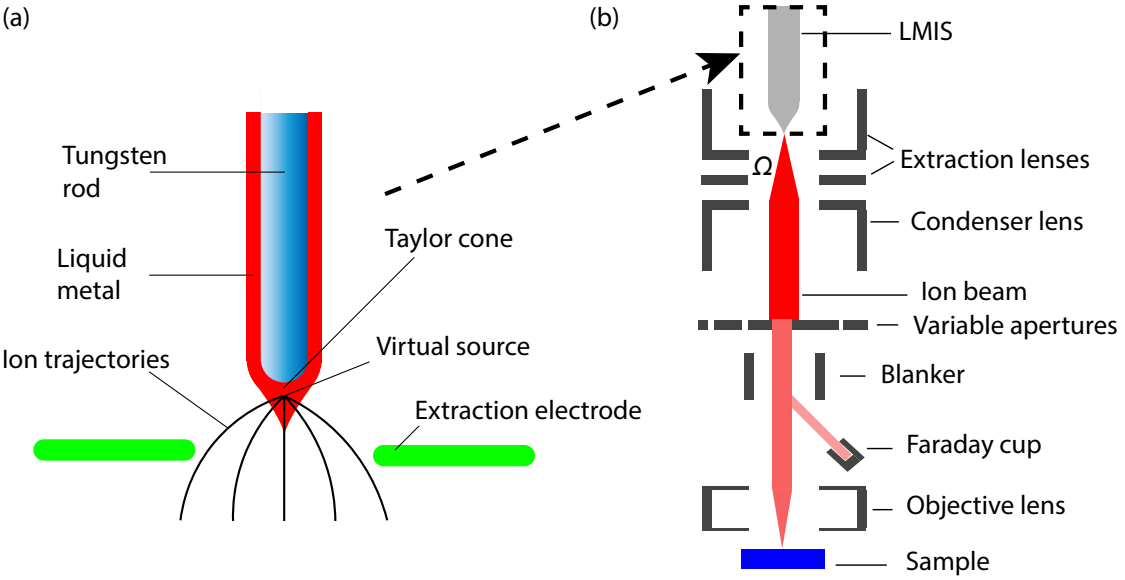

Figure 3.4: (a) Schematic depiction of a LMIS. The liquid metal surrounds a tungsten rod. Ions can be extracted from the liquid metal by applying a large potential. (b) Schematic overview of the optics used in a FIB. The beam is shaped by the objective lens, passes through the apertures to reduce the current and is subsequently focused onto the sample by the objective lens. Both figures adapted from ref [67].

Ions will be emitted from the LMIS in a solid angle Ω. To shape the beam and focus it on the sample, it has to pass through a series of electrostatic lenses and other optical elements. The optical path is schematically shown in figure 3.4b. The ions are extracted from the LMIS by the extraction lenses. Since this beam is divergent, a second lens, called the condenser lens, is required to shape the beam. Depending on the lens voltage, the beam can either be divergent, parallel or convergent, with crossover or focal point also dependent on lens voltage. Generally, focused

ion beams are operated with an initial parallel beam. Next, the beam travels through a set of apertures. Depending on the size of the aperture, part of the beam is blocked, reducing the total ion current in the beam. Before the beam hits the aperture, the beam currents are typically in the range of 1 to 5 μA. These currents are generally too large and will result in sample damage [63]. Hence the beam current is reduced by apertures to the order of 1 pA to 100 nA. Since for experiments it is often not desired that the beam always hits the sample, the beam can be diverted by the blanker lenses into a Faraday cup, which is used to measure the beam current. This lens basically acts as a quick on/off switch for the FIB. To focus the beam onto the sample, the objective lens is used. This lens is very close to the sample surface and is used to create a convergent beam with a focal point on the sample surface. The ion beam cannot be focused into an infinitesimally small point, since Coulomb interactions between individual ions in the beam limit the minimum distance between the ions. Generally the shape of the Ga^+ beam is Gaussian with a full width at half maximum (FWHM) down to a few nanometers and long tails, resulting in a Gaussian ion distribution at the FIB focus point. The ion beams that are used in this thesis, namely a FEI Nova Dualbeam SEM/FIB and an Orsay Physics Canion 31U ultra-high vacuum FIB, can reach spot sizes of roughly 5 nm at a beam current of 1 pA [67].

3.2.2 Ion-solid interactions

When high energy ions are shot at a surface they interact with the solid. These interactions will be discussed in this section, and are summarized in figure 3.5. The left image shows a typical Pt/Co/Pt sample structure with clear interfaces between the layers. Pt is shown in red and Co in blue. The high energy ions, in this case Ga^+ ions (shown in yellow), are shot towards the sample.

When the ion arrives at the sample, it will lose its kinetic energy due to collisions with the atoms and electrons in the sample. A distinction is usually made between elastic- and inelastic interactions [62]. Elastic interactions involve energy loss to the atoms in the solid. These interactions are covered in the collision cascade model, which describes these collisions as independent two-particle collisions. Due to conservation of momentum, atoms can be displaced from their original position in the crystal lattice if the transferred energy exceeds the critical displacement energy, as shown on the right in figure 3.5. The displaced atom can also displace another atom, hence the name collision cascade. If the displaced atom is near the surface, it can also be emitted from the surface, resulting in ion sputtering, as shown on the right in figure 3.5. Once the cascade has stopped, the remaining energy is lost to radiation and heat. In inelastic collisions, the ion will transfer its kinetic energy to the electrons. This results in the excitation of the electrons in the solid, as shown on the right in figure 3.5, which in turn can cause ionization or emission of x-rays or secondary electrons. Secondary electrons are generally used for imaging purposes. In these inelastic interactions, the total momentum is not conserved. Many factors influence the ion beam induced effects, namely the ion species (heaver ions have more momentum and travel further), ion energy (high energy ions take longer to lose their energy and thus can cause more damage), incidence angle, target species (lighter atoms are easier to displace) and target crystal structure [62].

As can be seen from the right image in figure 3.5, the resulting sample composition after Ga^+ irradiation is significantly different. Other than the increased disorder in atom distribution, the interfaces are also less well defined. Before Ga^+ irradiation the interface quality is very high with almost no fluctuations, while after Ga^+ irradiation the interface is significantly more disordered. The degree of disorder is often quantified with the amount of Ga^+ ions that hit the sample in a given area, often called the Ga^+ dose, with a larger Ga^+ dose resulting in a larger degree of disorder. In chapter 2 we showed that the fundamental magnetic parameters are dependent on the interface quality, and hence we can tune magnetic parameters with Ga^+ irradiation. We expect that the DMI strength D and effective anisotropy K_{eff} decreases with increasing Ga^+ dose, since they are heavily dependent on interface quality. Indeed, it has previously been reported that K_{eff}

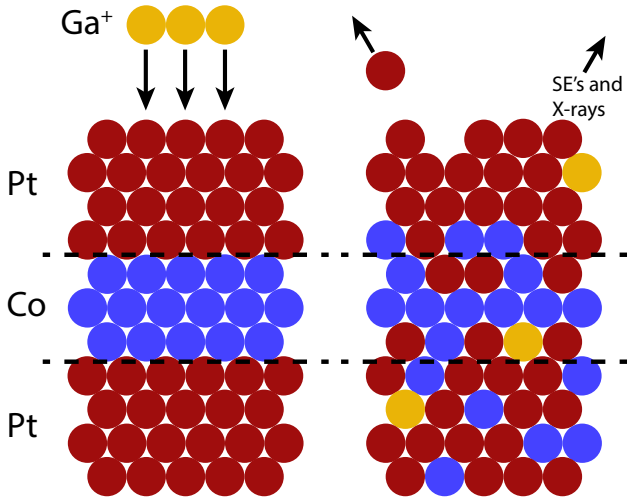

Figure 3.5: Effects of a focused ion beam on a layered Pt/Co/Pt sample. On the left, the sample is schematically drawn before irradiation by Ga ions. On the right, a multitude of effects are shown. The high energy Ga^+ ions can displace atoms, which will cause sputtering or intermixing between layers. They can also implant themselves into the sample and create secondary electrons or X-rays.

decreases with increasing Ga^+ dose [68, 69, 70, 60]. Franken *et al.* [60] quantified the change in K_{eff} with Ga^+ irradiation for Pt/Co/Pt wires with different Co thicknesses (0.4 - 0.6 nm). An exponential decrease in K_{eff} is observed with increasing Ga^+ dose. Research is currently ongoing on how D changes with Ga^+ irradiation, which will also be investigated in chapter 6. As mentioned in chapter 2, we assume that A and M_S are invariant with Ga^+ irradiation.

3.3 Micro-magnetic simulations

In chapter 4 we use micro-magnetic simulations to study skyrmion stabilization in confined geometries. Micro-magnetic simulations are used as a tool to describe experiments [71]. They use sample parameters and a given initial magnetization as an input and solve equations describing how the magnetization evolves over time to find the minimum energy state, which should also be obtained in the experiments. External influences and interactions, like the parameters discussed in chapter 2, can be switched on and off to determine which interactions are dominant. Many different micromagnetic simulation software packages exist [72], however for the simulations in this thesis we used MuMax^3 [73, 74] due to its ease of use and GPU acceleration, making it very fast.

All micromagnetic simulations approximate the magnetization with a vector field divided into cells. Cell sizes need to be smaller than the exchange length [28] $l_s = \sqrt{\frac{A}{\mu_0 M_S^2}}$ (roughly 2 nm in our samples) to obtain accurate simulations [75]. Furthermore, the outcome of the micro-magnetic simulations is very dependent on the initial magnetization. The solver can get stuck in a local energy minimum, which results in a different outcome than expected. Hence, a certain degree of caution needs to be exercised when interpreting the results of micro-magnetic simulations. The accuracy of the results can be increased by comparing the outcomes to experiments and theoretical predictions. Recipes for all the simulations performed in this thesis can be found in appendix A.1.

3.4 Sample Characterization Techniques

So far in this chapter we have discussed methods for fabricating, modifying and simulating our samples, but we have not yet discussed the sample characterization techniques. We will start by describing two imaging techniques, Kerr microscopy (section 3.4.1) and scanning electron microscopy with polarization analysis (SEMPA, section 3.4.2). Afterwards, we will briefly describe the SQUID-VSM method, which is used to measure the effective anisotropy and saturation magnetization of the samples.

3.4.1 Kerr microscopy

This section is based on an excellent description in refs [61] and [76]. Kerr microscopy makes use of the magneto-optical Kerr effect (MOKE) to image the magnetization of a material. MOKE can be described by a simple model of oscillating electrons in the magnetic material [77]. A beam of linearly polarized light hits the sample and the electric field of the light causes the electrons to start oscillating. Lorentz forces from the magnetization acting on the electrons add a perpendicular velocity component to the electrons, causing the polarization in the reflected light to rotate. The phase between the two velocity components can be used to extract the ellipticity of the reflected light. Both the polarization rotation and ellipticity scale linearly with the magnetization and hence can be used to measure the magnetization. In a Kerr microscope, the reflected light travels through a compensator and analyser, which isolate the polarization rotation. The measured intensity is then proportional the the polarization rotation, resulting in a different contrast for up and down domains. Different forms of Kerr microscopy can be used for in-plane or out-of-plane contrast, for more detail, please refer to refs [61, 76]. For the measurements in this thesis, only measurements for out-of-plane contrast are done.

Kerr microscopes can reach fields of view ranging from 1 cm to roughly 10 μm. The resolution of a Kerr microscope is only limited by the diffraction limit. Hence it is easily able to image the magnetic contrast in the 1×10 μm^2 Pt/Co/Pt wires used in chapter 5.

3.4.2 Scanning electron microscopy with polarization analysis (SEMPA)

Scanning electron microscopy with polarization analysis (SEMPA) has been used for over 20 years to study magnetic patterns at nanoscales. In this technique, which is schematically shown in figure 3.6a, a regular scanning electron microscope (SEM) is combined with an electron polarization detector, which allows us to investigate the spin of the secondary electrons in the reflected beam [20, 21, 22]. In a SEM, a focused electron beam is scanned across an area. Secondary electrons are created with similar processes as described for a FIB (section 3.2). Their spin is directly related to the in-plane magnetization in the sample. Secondary electrons are collected with electric fields and directed to a W(001) crystal, which has spin dependent diffraction spots due to spin orbit coupling. By placing electron counters at each diffraction spot for secondary electrons with spin in the +x, -x, +y, and -y directions, we can count how many secondary electrons with a certain spin are created at a certain spot at the sample, at typical resolutions on the order of 5 nm [22].

SEMPA can only probe the magnetization over a thickness of several nm, since secondary electrons from deeper in the sample will lose their spin information due to scattering. Hence, typical SEMPA samples do not contain capping layers. To prevent oxidation of the top magnetic layer or loss of spin information of the secondary electrons due to collisions with air molecules, SEMPA is typically conducted at ultra high vacuums, roughly 10^{-10} mbar. Furthermore, SEMPA cannot be used in applied magnetic fields, since the Lorentz forces from the magnetic field will disrupt the electron optics, as well as destroy the spin information of the secondary electrons.

In the following we will discuss how raw SEMPA data is converted into a full vector image of the magnetization. As an example, we will use a cylindrical 30 nm thick Co dot with a diameter of 3 μm. The expected magnetization in this dot is a vortex state, where the magnetization is perpendicular to the radius of the dot, due to its in-plane anisotropy and the minimization of stray fields (see chapter 2). Figures 3.6b - e show how the electron counts are processed into a magnetization image. By combining the counts from all detectors, a regular SEM image is obtained, shown in figure 3.6b. Here, we see the example Co(30) dot. By subtracting electron counts from opposite detectors (+x, -x, +y, and -y), information can be obtained for the magnetization components in either the x-direction (m_x, left and right detectors) or y-direction (m_y, up and down direction). This is shown in figures 3.6c and d for the m_x and m_y detectors respectively, where the geometry of the dot is outlined with an orange dotted line. In these figures, a clear contrast difference can be seen between the light and dark areas, corresponding to the direction indicated by the arrows on the top right of each image. Since figures 3.6b - d are created simultaneously, this information can be combined to extract the full magnetization $\boldsymbol{M}$ in the dot. This is shown in figure 3.6e, where the geometry of the dot is again outlined with a white dashed line. Here, the in-plane magnetization is color coded to the color wheel in the top right corner. Indeed, the Co dot contains a vortex magnetization state as was expected. This shows us that we can use SEMPA to extract the full in-plane magnetization profile of a sample. For samples with PMA, we can distinguish the up- and down domains by rotating the sample 5 - 10° with respect to the SEMPA roughly, which results in a projection of the out-of-plane magnetization on the in-plane measurement axis [78, 79].

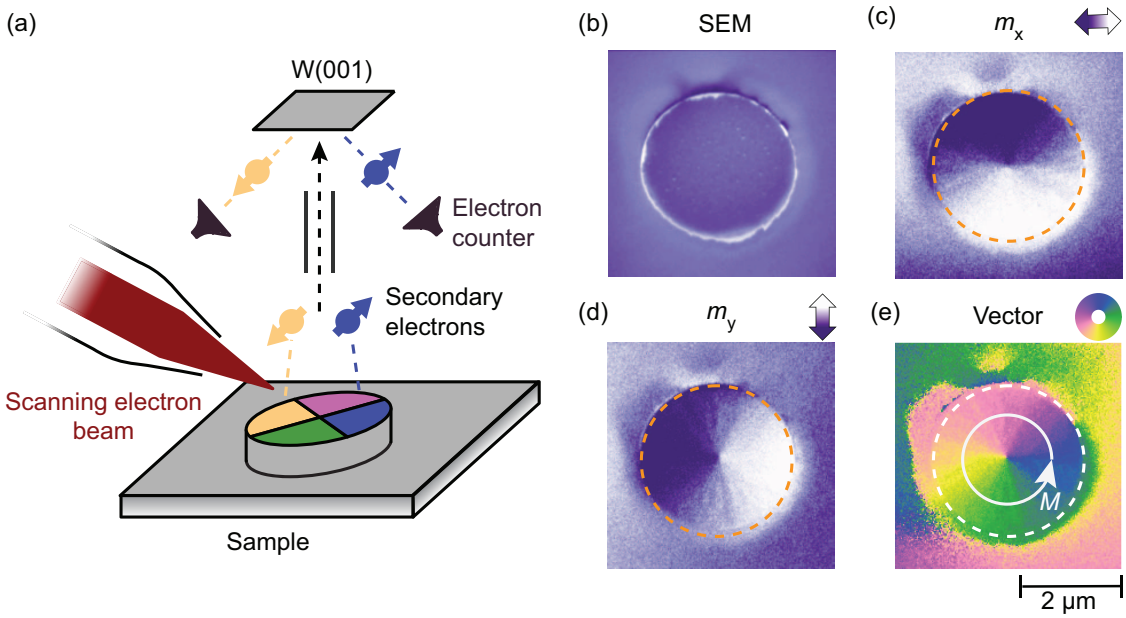

Figure 3.6: (a) Schematic overview of the working principles of the SEMPA, using a 30 nm thick Co dot with a vortex state as an example. An electron beam creates secondary electrons, with spin correlated to the magnetization in the dot. The secondary electrons scatter at the (001)W-crystal with spin specific diffraction spots, and travel to electron counters. (b)-(e) Example SEMPA analysis of the Co(30) dot. (b) Regular SEM image of the Co dot. (c) Magnetic contrast from the m_x detector. (d) Magnetic contrast from the m_y detector. (e) Composite image constructed from (c) and (d), with the magnetization color coded according to the color wheel. The vortex state is revealed. Image provided by ref [80].

3.4.3 SQUID-VSM

A superconducting quantum interference device with vibrating sample magnetometer, or SQUID-VSM, is a tool that can be used to measure the magnetization of a sample. A sample is quickly moved up and down by the VSM, which results in a changing magnetic flux. This is measured by the SQUID via Josephson junctions and can be converted into the magnetization of the sample. The exact working principles of the SQUID are outside of the scope of this thesis and hence will not be discussed further. For more information, please see ref [81]. By applying a magnetic field during the measurement sequences, a hysteresis loop ($\boldsymbol{M}$ as a function of $\boldsymbol{H}$) can be measured. From this hysteresis loop, K_{eff} and M_{S} can be extracted. In this thesis a SQUID-VSM from Quantum Design is used, which allows us to measure the magnetization at temperatures between 4 and 400K and in magnetic fields up to 7T. A major downside with SQUID is that this technique can only be used to measure the bulk magnetization, and cannot be used to resolve the local magnetization of areas irradiated with a FIB. Furthermore, SQUID-VSM is performed ex-situ, making it incompatible with the typical samples used in the SEMPA technique.

Chapter 4

Skyrmions in nanodots

In this chapter, we conduct an extensive set of micromagnetic simulations to investigate the stability of skyrmions in cylindrical $[\mathrm{Ir}(1)/\mathrm{Co}(0.6)/\mathrm{Pt}(1)]_{\mathrm{x15}}$ multi-layered nanodots, using MuMax^3 (see chapter 3). In chapter 1 we mentioned the use of a focused ion beam to create confined structures, which could be beneficial for the stabilization of skyrmions without application of a magnetic field, as required for SEMPA imaging.

Two types of simulations are performed; first we investigate the stabilization of skyrmions as a function of DMI strength and diameter of the nanodot. From this we gain insights into the required parameters to stabilize a skyrmion, without application of a magnetic field. However, skyrmions are a metastable state, or local energy minimum, instead of the ground state, or general energy minimum, since they are nucleated in external fields. Hence, the second set of simulations investigates the evolution of the magnetic structures in the nanodots as a function of applied magnetic fields. This gives us insights into the parameters required for nucleation of skyrmions in our samples, and allows us to compare the simulations to experiments [59]. Combining these results can give us the full overview of skyrmion nucleation and stabilization in our samples.

Before we can go into detail on the results of the simulations, we recall the energetics of nanodots from chapter 2 and describe the interplay between the interactions in the nanodots that define the ground state of the dot.

4.1 Nanodot ground states

All simulations in this chapter aim to minimize the total energy of the system. As mentioned in section 2.3, the ground state of these types of systems is determined by the interplay between the domain wall energy σ_{DW}, the Zeeman energy, the demagnetization energy and magnetic confinement as also reported by ref [26]. Examples of expected ground states are shown in figure 4.1, where the magnetization in the up and down directions is color coded with white and black respectively. The in-plane magnetization is color coded according to the color wheel, with the arrows denoting the direction of the magnetization corresponding to the color.

In figure 4.1a, a multi-domain state (MD) is shown. This state can result from a large dot diameter w, which we use to tune the demagnetization energy in the nanodot. A larger w adds more magnetic volume and thus increases the strength of the demagnetization energy, which is favorable for domain formation. Furthermore, decreasing the domain wall energy by increasing the DMI strength D also favors domain formation, since more domain walls will automatically result in more domains. A chiral labyrinth structure (c-LS), which is shown in figure 4.1b is expected

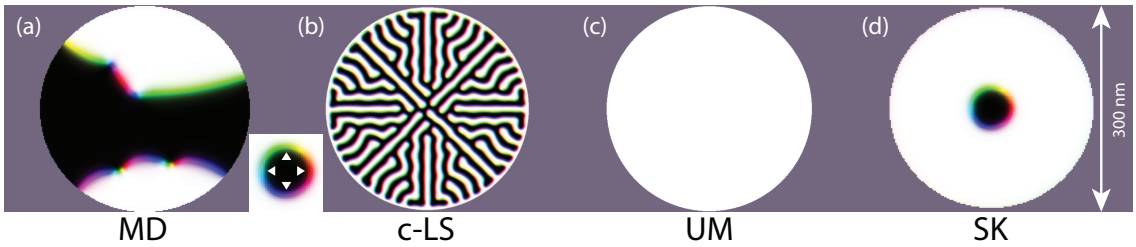

Figure 4.1: Possible ground states of the nanodots, depending on the strength of the magnetic interactions. The white and black colors denotes magnetization in the up- and down directions respectively, while the in-plane magnetization is color coded according to the color wheel. (a) A multi-domain state (MD), (b) a chiral labyrinth state (c-LS), (c) a uniformly magnetized state (UM) and (d) a Néel skyrmion (SK).

at large D, due to the negative σ_{DW}, meaning the system will form spin spirals (see chapter 2). A uniformly magnetized state, as shown in figure 4.1c is favored at large σ_{DW}, since A and K_{eff} are large and these interactions favor parallel alignment between spins, resulting in a UM state. Another interaction that favors parallel alignment between spins is the Zeeman energy, which prefers alignment with applied magnetic fields. Hence, at large Zeeman or domain wall energies, a UM state is expected. A skyrmion, as depicted in figure 4.1d, can be stabilized at intermediate values of the above described energies due to the skyrmion - edge interactions described in section 2.3.2. These interactions get stronger at smaller w [1].

In the micromagnetic simulations, the ground state was found to be strongly dependent on the initial conditions. If the initial condition is close to a local energy minimum, the micromagnetic solver can get stuck in such a local minimum, which results in simulation outcomes not depicting the ground state. The effect of various initial conditions on the final state of the nanodot has been investigated in appendix A.2. Using the results of appendix A.2, we can verify that the correct initial conditions are selected which result in the most accurate simulation outcomes. For the simulations regarding skyrmion stability (section 4.2), a Néel skyrmion was found to be the most suitable initial condition. For the simulations regarding the phase evolution of the nanodot in magnetic fields (section 4.3), random magnetization was chosen as the most suitable initial condition.

4.2 Skyrmions in confined geometries at zero field

Now that we have described the possible ground states of the nanodot, we can investigate the stability of skyrmions in nanodots in more detail. We will investigate the ground state of the nanodot as a function of the DMI strength D and w, since these parameters are favorable for skyrmion stabilization, as described in chapter 2. A and K_{eff} are kept constant at 10 pJ/m and 0.35 ± 0.03 respectively [27]. The saturation magnetization M_{S} is set at 1.0 ± 0.1 MA/m [27]. A Néel skyrmion is initialized in the nanodot, and the total energy is subsequently minimized for w values between 100 and 700 nm, and D values between 0.5 and 5.0 mJ/m^2. After energy minimization, the resulting phase is analysed for each combination of w and D values and plotted in figure 4.2. This method is analogous to the method by Ho *et al.* [26], and has been verified for our samples in appendix A.3. Details on the simulations such as mesh- and cell sizes can be found in appendix A.1. The colorbar on the right shows the color coding for the different phases in the phase diagram, corresponding to the phases shown in figure 4.1. The area in-between the dashed lines denotes a range of experimentally observed values for D [27].

[1] This effect is limited to the smallest w for which the other parameters allow a skyrmion to exist. At smaller w the exchange interaction and anisotropy will dominate, forming a UM state instead.

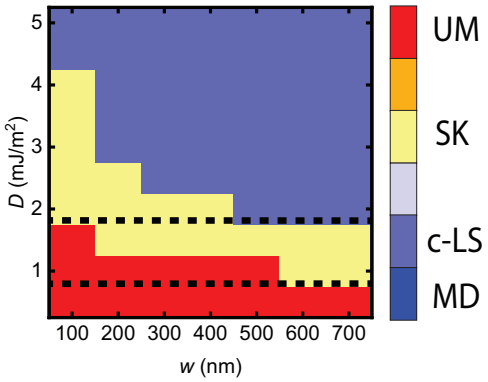

Figure 4.2: Simulated zero-field phase diagram of the $[Ir(1)/Co(0.6)/Pt(1)]_{15}$ nanodots. The colorbar on the right shows the color coding for the different phases in the phase diagram, corresponding to the phases shown in figure 4.1. The area inbetween the dashed lines denotes a range of experimentally observed values of D for this stack [27].

In figure 4.2, three distinct phases are present for the simulated window of w and D. At high D, the c-LS state is present, which transitions into the SK and UM phases for decreasing D. At high w, lower values of D are required to stabilize a SK or c-LS state due to the increase in dipolar energies. The MD state does not show up at the largest w investigated, which is likely caused by relatively weak dipolar interactions compared to the domain wall energy, combined with the initial condition. However the MD state is expected to be stable at $w > 700$ nm, where the dipolar energy is strong enough. At lower w, the UM phase is stable for larger D values, since the influence of the dipolar energy is smaller. Also, in this regime the SK phase is more stable for a larger D window, due to the skyrmion-edge interactions resulting from the confinement. The results in figure 4.2 are consistent with the expectations of section 4.1 and indicate that there is a regime of D and w values where skyrmions are stabilized in our samples. From figure 4.2 can also be concluded that the SK phase is stable in the range of observed D values for of our stack, especially at larger diameters.

4.3 Nanodot phase evolution in applied magnetic fields

So far, the simulations assumed that a Néel skyrmion is already present in the sample, but experimentally this is not always the case. Generally Néel skyrmions are a metastable state and not the ground state of the nanodot. Experimentally, this state is often achieved by applying a magnetic field. Hence, to get the full picture of skyrmion stabilization, the phase evolution in external magnetic fields is studied in this section. This gives us insights on the required parameter window to nucleate skyrmions.

As described in chapter 2, skyrmions are generally nucleated from either a MD state ($D < D_{\mathrm{crit}}$) or a c-LS state ($D > D_{\mathrm{crit}}$), where $D_{\mathrm{crit}} = \frac{4}{\pi}\sqrt{AK_{\mathrm{eff}}}$ is the critical DMI value for which σ_{DW} becomes negative and the system will host as much domain walls as possible. By applying a magnetic field, the Zeeman energy is increased, which causes the system to form skyrmions to retain as much DMI energy while gaining Zeeman energy. For $D < D_{\mathrm{crit}}$, the skyrmions show up as isolated particles surrounded by a multi-domain structure [18], while for $D > D_{\mathrm{crit}}$, the system will form a lattice [11]. At very high magnetic fields, it is no longer worthwhile for the system to form skyrmions and hence to maximize its Zeeman energy, a UM state will be formed (as mentioned in section 4.1). We expect that the phase evolution in our dots follows a similar

phase evolution, due to the factors described above.

To verify if this hypothesis is correct, a high energy state is initialized in the dot in the form of random magnetization. This state is allowed to relax to form a MD state in the dot, since after relaxation of this condition the resulting ground states best matched experimental observations [59]. From the ground (MD) state, an increasing magnetic field is applied in the z-direction, until the sample is saturated. At each field step, the energy is minimized and the phase of the nanodot is analyzed. This process is repeated for w between 100 and 700 nm. Values for A, K_{eff} and M_{S} are the same as in section 4.2. Values of D for this stack were measured to lie between 1.0 $\pm$ 0.3 mJ/m^2 ($\sim 0.42 D_{\text{crit}}$) and 1.7 $\pm$ 0.2 mJ/m^2 ($\sim 0.71 D_{\text{crit}}$) by ref [27]. To verify whether skyrmions are nucleated with an external magnetic field in our samples, we conduct simulations at those values, as well as at the critical DMI value $D_{\text{crit}} = 2.38$ mJ/m^2 to investigate the nucleation process at high D values. Details on these simulations can be found in appendix A.1.

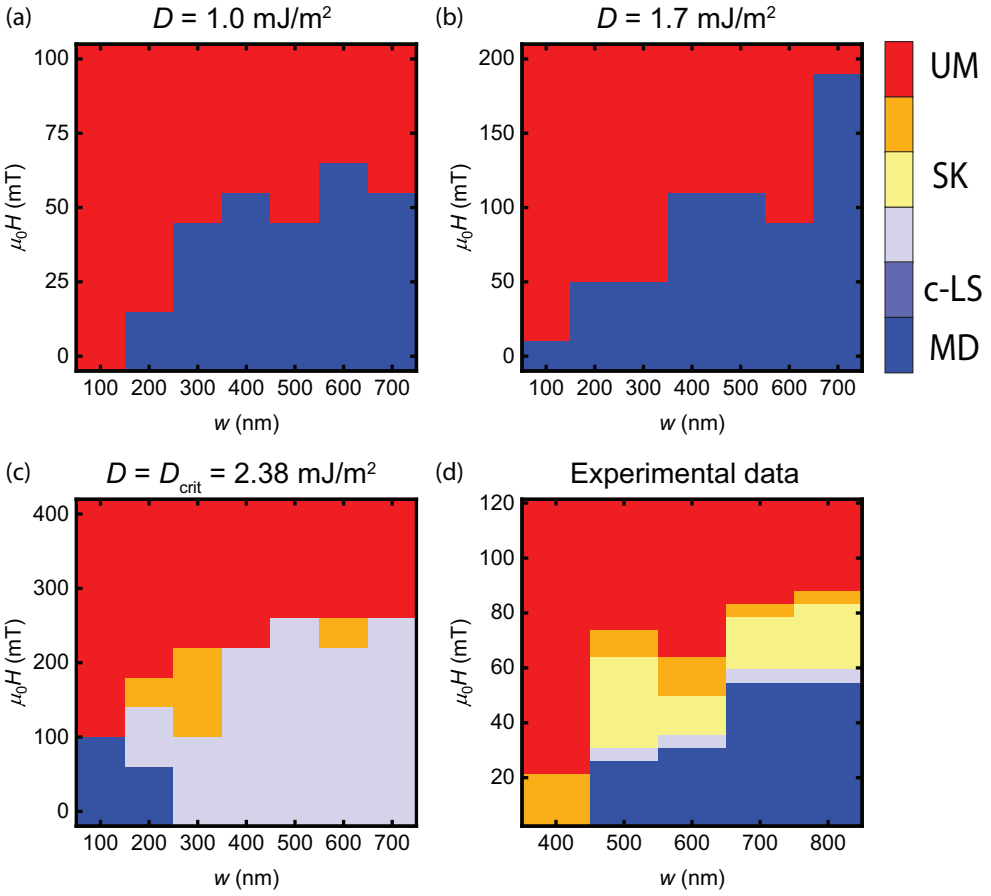

Figure 4.3: Field evolution phase diagrams. (a)-(c) are simulated phase diagrams for respectively $D = 1.0$ mJ/m^2, 1.7 mJ/m^2 and $D = D_{\text{crit}} = 2.38$ mJ/m^2. (d) Experimental data by ref [59].

Figure 4.3a shows the phase evolution of the nanodot for $D = 1.0$ mJ/m^2, with the colors indicated the phase of the nanodot. At low w, the system is already in the UM phase and hence applying a magnetic field does not change the phase. For larger w, the ground state of the dot is a MD state, which transitions at larger fields into the UM state due to the increase in Zeeman energy. For all w, the transition from MD into UM is direct and does not involve the stabilization of skyrmions as described in the process above. This is also the case for the simulations where $D = 1.7$ mJ/m^2, shown in figure 4.3b. The MD phase persists at larger magnetic fields and smaller diameters than in the case of $D = 1.0$ mJ/m^2, due to the lower energy cost to form domain walls. However likewise

to the case of $D = 1.0$ mJ/m^2, no skyrmions are predicted to form. Only when $D = D_{\text{crit}}$ chiral structures are stabilized, as shown in figure 4.3c. The phase transitions from a MD to a mixed MD + SK phase for larger w, which transitions either directly or via a mixed SK + UM state into a UM state. Figure 4.3d shows experimental data from ref [59], where the magnetic structure of dots is investigated for increasing magnetic fields with a magnetic force microscope [82] for w between 400 and 800 nm. Comparing these results to figures 4.3a-c shows a similar behavior in the low- and high field limits. The MD state is stabilized around similar values for the case where $D = 1.0$ mJ/m^2, and both similar values for the UM state. However, in the experimental data the predicted transition from MD to SK to UM is observed, while for the simulations in figures 4.3a and b no chiral structures are observed.

The absence of chiral structures in the simulations can be the result of the following factor. Variations in K_{eff} and D due to interface roughness can create pinning sites, where metastable skyrmions can locally be created. Variations in D have been observed to be as large as 75% for similar samples [83]. In the simulations in this chapter, local variations in K_{eff} and D are not considered, which can result in chiral structures not being stabilized in our simulations. Hence to more accurately describe skyrmion nucleation in experiments, this variation of parameters has to be taken into account.

In conclusion, in this section we investigated the nucleation of skyrmions in nanodots. We found decent agreement for the magnetic phase of the nanodot with experimental observations for the low- and high field limits, however we did not observe any skyrmions in our simulations. This was mainly caused by the fact that large parameter fluctuations due to interface roughness were not considered in the simulations.

4.4 Summary and Outlook

In this chapter, we investigated the stability and nucleation of skyrmions in nanodots. Stable skyrmions in nanodots in zero field are required for imaging in SEMPA, which is the ultimate goal that we work towards in this thesis.

In section 4.2, we investigated the stability of a skyrmion for a range of DMI values and dot diameters, to find a regime where skyrmions are stabilized for our samples. We found that skyrmions are stabilized for experimentally observed values in our samples. However, due to the metastability of the skyrmion state, their nucleation has to be observed as well. Experimentally this is often done with a magnetic field. Hence, in section 4.3, we investigated the evolution of the magnetic phase in the nanodots in a magnetic field. There we found good agreement in the limits of high and low magnetic fields, however no skyrmions were observed. The main cause of this issue are the fluctuations in D and K_{eff} which are present in sputtered samples, and not taken into account in the simulations. To further improve this data, these fluctuations have to be taken into account.

An important note to make is that the simulated nanodots in this chapter represent physical skyrmion confinement, while FIB induced confinement can either provide confinement through a magnetic dot surrounded by a magnetically dead region [84] or regions with in-plane magnetization. While these forms of confinement are expected to give similar results (tilting of spins at the edge is still expected to occur, see chapter 2), this has to be verified in future simulations and experiments.

Furthermore, a focused ion beam could also be used to enhance skyrmion stabilization. It has already been proven that Ga^+ irradiation can decrease K_{eff} [60], and research is currently ongoing on its effect on the DMI [27, 85, 86, 87], which in this thesis is also investigated in chapter 6. Lowering K_{eff} is a method for decreasing the critical DMI value required to stabilize chiral structures. Hence, lowering K_{eff} is expected to shift the regime where skyrmions are stabilized to lower D values in figure 4.2. However, because the effect of ion irradiation on the DMI and other parameters is still not fully known, its effectiveness as a tuning tool to enhance skyrmion stabil-

ization is to be seen. Significant insights on the viability of ion irradiation for tuning skyrmions stabilization can be gained if the changes in K_{eff}, A, M_{S} and D can be quantified.

To be able to quantify the changes in K_{eff}, A, M_{S} and D due to Ga^+ irradiation, the in-situ FIB that we are using in this thesis (see chapter 1), first has to be calibrated. In chapter 5, we discuss this calibration. After this is done, the effects of Ga^+ irradiation on magnetic properties are investigated in chapter 6.

Chapter 5

FIB calibration: domain wall injection

As mentioned in chapter 1, we need to calibrate the in-situ FIB Ga^+ dose before we can do quantitative measurements with it. In this chapter we will do so by comparing experimental results with a different FIB, whose dose is well known. We also investigate how we can control the resolution of the FIB, which is vital to know if we want to create structures on the nanometer scale with FIB.

The method that we will use in this chapter is *domain wall injection*, and it is based on an experiment performed by Franken *et al.* [60]. In this experiment, half of a Pt/Co/Pt wire with perpendicular magnetic anisotropy (PMA, see chapter 2) is irradiated with Ga^+ ions, shown in figure 5.1a, with the irradiation areas drawn in white boxes. This creates an anisotropy barrier in the wire [60]. A schematic drawing of a single irradiated wire is shown in figure 5.1b, where the arrows indicate the direction of the magnetization in each area. The width of the anisotropy barrier between the irradiated areas is denoted by δ. The size of this barrier, $K_{\text{eff},0} - K_{\text{eff}}$, where $K_{\text{eff},0}$ is the anisotropy of the unirradiated area and K_{eff} the anisotropy of the irradiated area, is dependent on the Ga^+ dose. In this chapter, we investigate the external magnetic field required to switch the magnetization in the un-irradiated area, which is dependent on the size of the anisotropy barrier and the anisotropy of the irradiated area, and thus the Ga^+ dose. By comparing results of these magnetic field measurements between two different focused ion beams, we can calibrate the unknown dose from the in-situ FIB. In the next section, we go into more detail on the basic principles of the experiment. After the basic principles have been established, the calibration results will be discussed.

5.1 Domain wall pinning and nucleation control

In this section, we describe the principles of controlling domain wall nucleation and pinning using Ga^+ irradiation. In the experiment, we measure the magnetic field required to move a domain wall over the energy barrier, defined as the *injection field* H_{inj}. H_{inj} depends on the balance between the *domain wall nucleation field* H_{nucl}, defined as the field required to create a domain wall in the irradiated area, and H_{depin}, defined as the field to move a domain wall over an anisotropy barrier [60].

The strength of H_{nucl} is dependent on the anisotropy of the irradiated area K_{eff}, since the energy required to form a domain wall is dependent on K_{eff} (see chapter 2). A lower effective anisotropy

means a lower domain wall energy and thus it is easier to nucleate a domain wall. This means decreasing K_{eff} by Ga^+ irradiation will decrease H_{nucl}. For anisotropy barriers where both the irradiated and the un-irradiated areas retain their PMA and hence have positive K_{eff}, the strength of the depinning field is given by [60]

$$H_{\text{depin}} = \frac{K_{\text{eff},0} - K_{\text{eff}}}{2\mu_0 M_S}, \tag{5.1}$$

where $K_{\text{eff},0} - K_{\text{eff}}$ represents the size of the anisotropy barrier. This means decreasing K_{eff} by Ga^+ irradiation will increase H_{depin}. For anisotropy barriers where the irradiated area has negative, in-plane, effective anisotropy, the depinning field is given by [60]

$$H_{\text{depin}} = \frac{K_{\text{eff},0}}{\mu_0 M_S}. \tag{5.2}$$

Here, the depinning field is unaffected by Ga^+ irradiation, since it is not dependent on the anisotropy of the irradiated area. From the balance between H_{depin} and H_{nucl}, we can identify three regimes. The switching behavior of these regimes is schematically visualized in figures 5.1c.

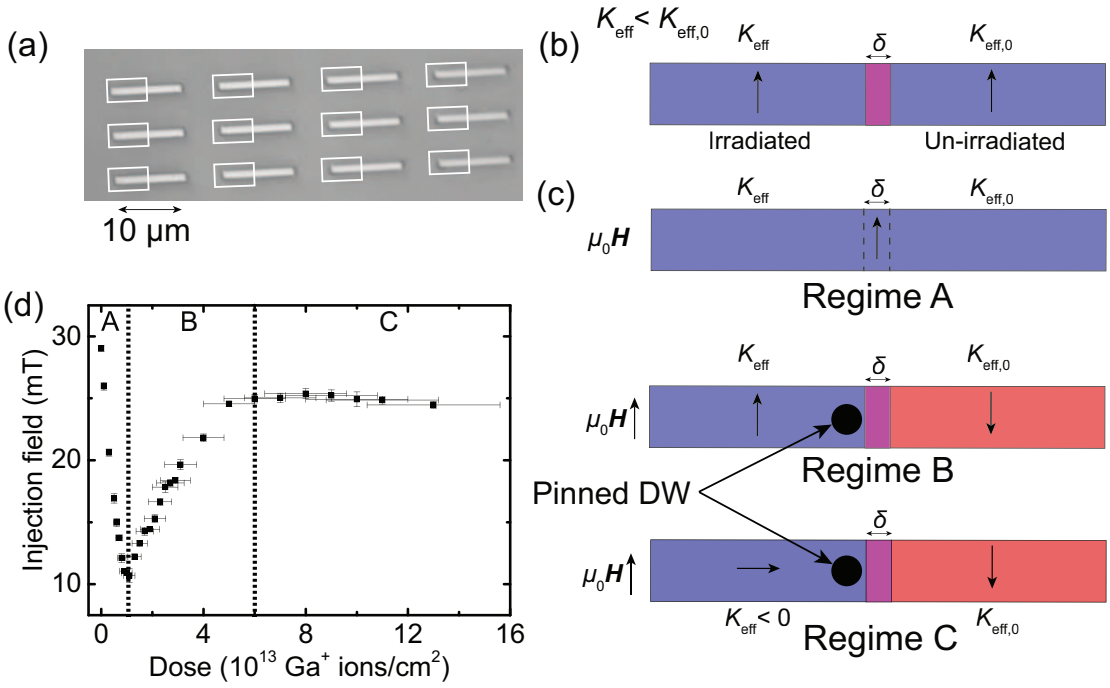

Figure 5.1: (a) Kerr microscopy image of the Ta(4)/Pt(4)/Co(0.6)/Pt(4) nanowires, with irradiation areas drawn in white boxes. (b) Schematic drawing of a wire after irradiation, where δ is the width of the anisotropy barrier. The arrows denote the direction of $\vec{M}$. (c) Schematic drawing of switching behavior in regimes A, B and C respectively. In regime A, the entire wire switches at once, because the anisotropy barrier is too small to pin a domain wall. In regime B, only the irradiated area switches, but a domain wall, visualized by a black dot, is pinned at the anisotropy barrier because the applied field is not strong enough to overcome it. In regime C, the irradiated area has a negative anisotropy, and hence has in-plane magnetization. The applied magnetic field is not strong enough to switch the un-irradiated area. (d) Domain wall injection measurements on Ta(4)/Pt(4)/Co(0.6)/Pt(4) wires, with each regime indicated in the figure. The transitions between the regimes are indicated with dashed lines.

In the first regime, $H_{\text{nucl}} > H_{\text{depin}}$. In this case, the domain wall is created at a field which is larger than the depinning field. Thus, the domain wall will immediately be able to jump over the anisotropy barrier once it has been created, and hence $H_{\text{inj}} = H_{\text{nucl}}$. We will call this regime A. In the second regime, $H_{\text{depin}} > H_{\text{nucl}}$. In this case, the domain wall, visualized with a black dot, is created in the wire, but the field is not strong enough to help the domain wall over the energy barrier. Only once the applied field reaches the depinning field, the domain wall will move over the energy barrier. This means that $H_{\text{inj}} = H_{\text{depin}}$. We will call this regime B. In the last regime, we describe the transition at an in-plane to out-of-plane barrier. Here, the depinning field dominates like in regime B, but remains constant according to equation 5.2. Hence, $H_{\text{inj}} = H_{\text{depin}} = \text{constant}$. We will call this regime C.

By looking at the changes in H_{nucl} and H_{depin} as a function of Ga^+ irradiation, we can predict how H_{inj} changes with increasing Ga^+ dose. For low doses, the size of the anisotropy barrier is too small, hence the injection field will be dominated by the nucleation field. Since we decrease K_{eff} with Ga^+ irradiation and thus also H_{nucl}, we expect to see a decrease in the injection field, which means we are in regime A. However, at larger doses, the anisotropy barrier becomes significant and we are in regime B where H_{depin} is dominant. Here we predict an increase in H_{inj}, since a higher Ga^+ dose results in lower K_{eff}, resulting in a larger barrier and thus larger H_{depin} (see chapter 2). We expect H_{inj} to keep increasing until the irradiated area has in-plane anisotropy (regime C). Since the depinning field is constant in this regime (see chapter 2), we expect H_{inj} to stay constant for increasing Ga^+ dose.

To verify our predictions, experimental data for 10×1 μm^2 wires of Ta(4)/Pt(4)/Co(0.6)/Pt(4) (thickness of each layer between brackets in nm) is gathered. The switching behavior of the wires in an applied magnetic field is analyzed using a Kerr microscope (see chapter 3). 12 wires with the same dose have been analyzed to achieve good statistics. A recipe for the wires can be found in appendix B. The resulting injection field as a function of Ga^+ dose is shown in figure 5.1d. Transitions between regimes A, B and C are indicated by dashed lines. The expected behavior described above is clearly visible. We see a decrease of H_{inj} in regime A with increasing Ga^+ irradiation. At larger doses we see a transition to regime B, where we see the expected increase of H_{inj} with increasing Ga^+ irradiation. At very large doses (in regime C), we see a clear saturation of H_{inj} at a constant value, which is as expected.

The magnitude of the measured injection field is significantly lower than the values predicted by the model described in chapter 2 and ref [60]. At zero dose, the wire should switch at the anisotropy field $H_{K_{\text{eff}}} = \frac{2K_{\text{eff},0}}{\mu_0 M_S}$, and according to equation 5.2, H_{depin} should be half the value of the anisotropy field at zero dose. For the samples in this chapter, we found values of $\mu_0 H_{K_{\text{eff}}} = 1.8\text{T}$ and $\mu_0 H_{\text{depin}} = 0.9\text{T}$. Here we used $K_{\text{eff}} = 1.1$ MJ/m^3 and $M_S = 1.2$ MA/m, obtained from SQUID-VSM measurements (see chapter 3), which are in accordance with literature [88]. These values are a lot higher than what is measured in figure 5.1d. However, only perfect systems that can be described with a Stoner-Wolfarth [28] model switch at the anisotropy field. In experiments, switching behavior is dominated by nucleation at random defects [89] and thermal effects [90]. This means the observed value of the injection field in regime A will be significantly lower, due to the decreased nucleation field. The switching in regime C is not dominated by nucleation, but by domain wall depinning. Domain wall depinning is likewise affected by higher temperatures [91], hence it is normal to measure significantly lower injection fields. We also expect that defects do not play a significant role in domain wall depinning, which can explain why we measured higher than expected injection fields in regime C (higher than half the fields at zero dose).

We can use the results from figure 5.1d as a calibration tool for the dose of the in-situ FIB, by comparison with results from a pre-calibrated FIB (in this thesis a FEI Nova dualbeam SEM/FIB, denoted by DualBeam in the remainder of this thesis). This will be discussed in the next section.

5.2 FIB calibration with domain wall injection

Before we can discuss the calibration results, we have to take the sample quality into account. Sample quality has a large impact on the quantitative aspect of the results, because fluctuations in thickness, caused by variations in the sputtering process, impact the effective anisotropy [1]. Hence, to accurately compare the results of two different focused ion beams, the samples have to be prepared and measured in exactly the same way, up to the irradiation step. During the sample fabrication process, the EBL, sputtering and lift-off steps have been performed in the same conditions. A recipe for the sample fabrication steps can be found in appendix B.

The dose from the in-situ FIB can be calculated from parameters in the software. We use this calculation as an estimate for the actual in-situ FIB dose, which will be compared to the pre-calibrated dose from the DualBeam. We use the following expression as an estimate for the in-situ FIB dose:

$$D_{\text{base}} = \left(\frac{N_{\text{pixel}}}{F}\right)^2 \cdot I_{\text{b}} \cdot t_{\text{irr}}, \tag{5.3}$$

where N_{pixel} is the amount of pixels on the x-axis, F the field of view, which denotes the length of the axis, I_{b} the beam current and t_{irr} the dwell time per pixel. The first part of the expression has to do with the size of the irradiated area, while the second part of the expression has to do with the amount of Ga^+ ions hitting the sample. Please refer to appendix C for more information on how this dose is calculated.

Now that we have established a method to calculate the in-situ dose, we can compare this to the dose of a known FIB by doing domain wall injection measurements on wires irradiated with both FIBs. We do this by performing a linear regression in regime A of the domain wall measurements since domain wall injection is dominated by nucleation in this regime, which is not influenced by δ [60]. Hence compare the slopes of the fits in regime A to see if our dose calculation is accurate, regardless of beam quality (which is linked to δ).

In figure 5.2, the domain wall injection results, including fits in regime A, for both the DualBeam (figure 5.2a) and in-situ FIB (figure 5.2b) are shown. The value of the slope is also shown in each figure. The dashed lines denote the transitions between regimes, with line 1 denoting the transition between regimes A and B and line 2 denoting the transition between regimes B and C. It can be concluded that qualitatively, the two measurements show a similar behavior. All three regimes are visible for both measurement sets, with a sharp decrease of H_{inj} in regime A, an increase in regime B which saturates to a stable value in regime C. From the fits in figure 5.2 can be concluded that, although there is a difference in the slopes, they are in the same order of magnitude, which suggests there is decent agreement between the two calculation methods. From this, we gain confidence in the fact that the method for calculating the Ga^+ dose from the in-situ FIB is accurate, especially for lower dose ranges. The experiments in the remainder of this thesis all use doses in this range.

To further improve the dose calculation, improvements can be made in determining the quantities used in equation 5.3. N_{pixel} and F are now determined by the software, but their accuracy can be improved by using structures whose dimensions are known for reference. By implementing these improvements, the agreement between the slopes in figure 5.2 should improve and hence the dose calculation for the in-situ FIB should become more accurate.

[1] The effective anisotropy is dependent on the thickness of the magnetic layer, see chapter 2.

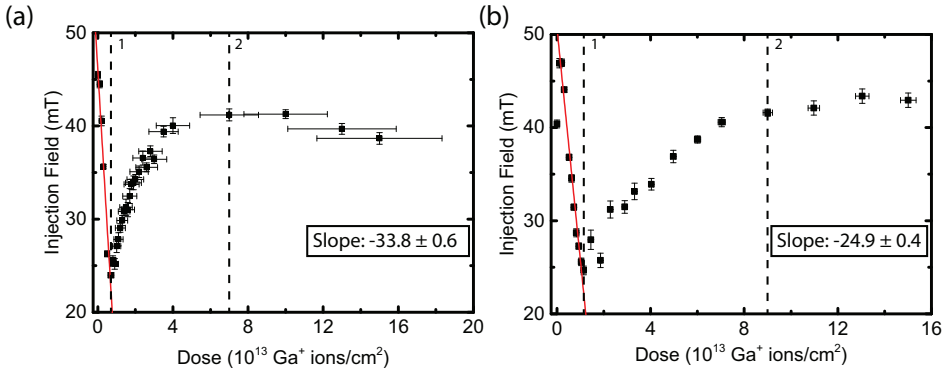

Figure 5.2: Domain wall injection measurements for (a) the DualBeam and (b) the in-situ FIB, including fits in regime A and the values of the slope of the fit. In both figures, the dashed lines denote the transitions between regimes, with line 1 denoting the transition between regimes A and B and line 2 denoting the transition between regimes B and C.

5.3 Resolution control with Ga^+ irradiation?

Another observation that can be made when comparing figures 5.2a and b is that for the in-situ FIB, H_{inj} does not increase as fast in regime B as for the DualBeam data. This is indicative for an increased anisotropy barrier width δ, according to ref [60]. If δ is larger, H_{inj} will be lower for that particular dose. Hence, the observed increase in regime B for the in-situ FIB data indicates a larger average δ, and also beam, for the in-situ FIB than for the DualBeam [60]. δ is linked to the resolution of the beam, since a larger (un-focused) beam increases δ [60]. We can use this to compare the beam resolution between the two FIBs, which will be investigated in more detail in this section. This is important to know if we want to create nanometer scale structures with FIB. We do so by conducting domain wall injection experiments with a purposely defocused beam and comparing the results to domain wall injection measurements with optimal focus.

From previous experiments, we already know it is possible to tune δ using the DualBeam by defocusing the ion beam [60]. Hence in this experiment we use the same method to achieve a larger δ. In the in-situ FIB, the size of the pixels can be tuned in the software. This artificially tunes δ, since larger pixels result in a beam that is spread out over a larger area (which should result in a larger δ) [2]. Note that the beam is not directly defocused by this method, but instead artificially defocused.

Results from the domain wall injection measurements are shown in figure 5.3, with the DualBeam data shown in figure 5.3a and the in-situ FIB data shown in figure 5.3b. The transitions between regimes are indicated with dashed lines, where lines 1 and 1' show the transition between regimes A and B and lines 2 and 2' show the transition between regimes B and C. Lines 1 and 2 regard the transitions for the optimally focused measurements, while lines 1' and 2' regard the transitions for the (artificially) defocused measurements in each figure. Figure 5.3a shows a stronger decrease in regime A for the defocused measurements. Furthermore, in regime B the range over which the injection field increases is larger, and regime C is absent altogether in the Ga^+ range investigated for the defocused measurements. Figure 5.3b shows similar behavior, but less extreme. Only a small increase of the range in regime B is observed. This behavior is as expected with a larger δ [60], indicating that δ is indeed larger for a(n) (artificially) defocused beam than for an optimally focused beam. The defocus is not quantified in the case of the DualBeam (fig 5.3a), hence a value of δ cannot be extracted. However, by comparison with simulations from ref [60], δ is estimated

[2] This is only valid if there is enough overlap of the beam between the pixels to create a homogenous irradiation area.

to be on the order of 100 nm. In the case of the in-situ FIB data (fig. 5.3b), the increase on pixel size, which effectively spreads out the beam, is roughly 61%, but this is not directly convertible to a δ increase. However, by comparison with simulations, δ is estimated to be on the order of 20-80 nm for the artificially defocused measurements.

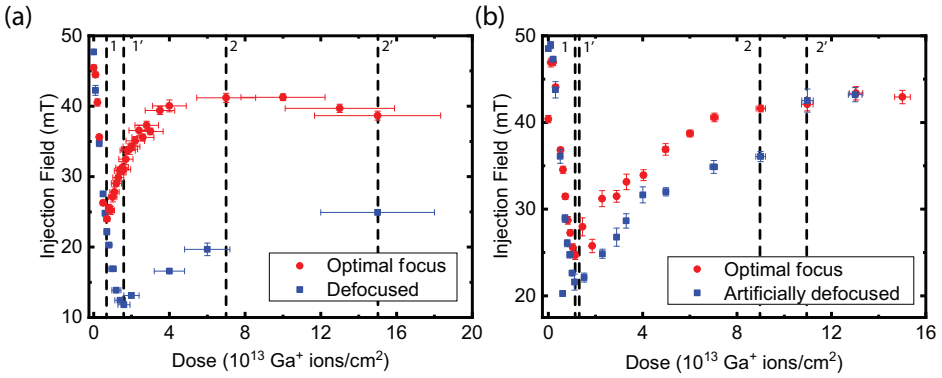

Figure 5.3: Domain wall injection data investigating the possibility of tuning δ with the (a) Dualbeam, by defocusing the beam and (b) in-situ FIB, by (artificially) increasing the size of the beam in the software. The transitions between regimes are indicated with dashed lines, where lines 1 and 1' show the transition between regimes A and B and lines 2 and 2' show the transition between regimes B and C. Lines 1 and 2 regard the transitions for the optimally focused measurements, while lines 1' and 2' regard the transitions for the (artificially) defocused measurements.

In conclusion, we found that δ and thus the resolution can be tuned for both FIBs. In the DualBeam this is difficult to do quantitatively, but we found similar behavior to the literature. For the in-situ FIB, we can tune the probe size in the software which results in a different δ, although no direct conversion could be made. The in-situ FIB is favorable for tuning the resolution in this situation, since the beam parameters can be adjusted more quantitatively. For both FIBs δ is only slightly smaller than the confined structures which were investigated in chapter 4, which limits the size of the structures that can be made with the FIB. To gain a more accurate picture of resolution tuning in the in-situ FIB, more measurements with different δ have to be performed. An accurate conversion between δ and the resolution also needs to be made to fully understand how the resolution can be tuned with the in-situ FIB.

5.4 Summary

In this chapter, we described the process of calibrating the in-situ FIB with domain wall injection experiments, by comparing results with a pre-calibrated FIB. In section 5.1, we explained how we can experimentally control domain wall nucleation and pinning using Ga^+ irradiation. In section 5.2, we discussed the calibration results for the in-situ FIB. We found that our calculation method for the in-situ FIB dose is in good agreement with the pre-calibrated FIB dose, especially for small doses.

In section 5.3, we investigated the effect of changing the anisotropy barrier width δ and its effects on the resolution in more detail. We found that δ can be changed by defocusing the beam in the DualBeam and by changing beam parameters in the in-situ FIB. We found that the resolution, which is linked to δ, is similar to, or slightly smaller than, the smallest investigated structures in chapter 4, which limits the minimum size structures that can be made.

Chapter 6

Tuning magnetic parameters with Ga^+ irradiation

In chapter 1, we proposed the use of a FIB to introduce confined structures that can aid skyrmion stabilization. Inducing confinement is not the only way a FIB can be used to stabilize skyrmions. By irradiating samples with Ga^+ ions, magnetic parameters like the effective anisotropy K_{eff} can be changed [60] (see also chapters 3 and 5). This could be favorable for skyrmion stabilization, since a reduction in K_{eff} results directly in a reduction in domain wall energy (see chapter 2). However, the effects of Ga^+ irradiation on other parameters relevant for skyrmion stabilization like the DMI D, saturation magnetization M_S and exchange stiffness A are unknown and are still subject of current investigations [27, 85, 86, 87, 92]. Most of these investigations consider only single layered systems (e.g. W/CoFeB/MgO) [85, 86, 92], and research is currently being conducted on multi-layered samples [27, 87].

In this chapter, we aim to add to this research by investigating the changes in magnetic parameters of Ta(4)/Pt(2)/[Pt(1)/$Co_{80}B_{20}$(0.7)/Ir(1)]$_{x6}$/Pt(1)/$Co_{80}B_{20}$(0.8) (thicknesses indicated between brackets in nm) multi-layered samples due to Ga^+ irradiation. For this investigation, we use a scanning electron microscope with polarization analysis (SEMPA, see chapter 3), which until now has never been used to study samples that are irradiated with Ga^+ ions. SEMPA allows us to study not just the domain structure, but also individual domain walls (see chapter 2). On the scale of magnetic domains (μm scale, e.g figure 6.1a), we look at the changes in domain size, which can be used in models [47, 93] to extract changes in D. On the scale of domain walls (nm scale, an example shown in white in figure 6.2b), we will investigate two properties. First, we will investigate changes in the average domain size, which allows us to extract changes in K_{eff}. Second, we will introduce a new experiment, based on changes in domain wall chirality (see section 2.2.2), which will allow us to investigate changes in D.

6.1 Effect of Ga^+ irradiation on domains

In this section, we attempt to investigate the changes in the individual magnetic parameters by investigating the domain size as a function of Ga^+ dose. We specifically focus on the changes in D, due to its importance in skyrmion stabilization. As mentioned in chapter 2, the domain size is dependent on the balance between the exchange interaction, anisotropy, demagnetization, DMI and Zeeman energies. Hence, by investigating changes in the domain size, we investigate the changes in all these interactions by Ga^+ irradiation. To untangle the individual changes in these parameters, we can make use of a model by Draaisma and de Jonge [47] to extract changes in D.

The model by Draaisma and de Jonge describes the domain size resulting from the competition between the demagnetization energy and the domain wall energy, from which we can extract D. By calculating D at each Ga^+ dose from this model, we can investigate how D changes with Ga^+ irradiation. For this model, we need values for A and M_S, which we define at 12 pJ/m and 0.49 MA/m respectively. So far, no A value for CoB has been reported. Since we use CoB instead of Co, we take A slighly lower than the conventional 16 pJ/m that is assumed for Co, because of the reduced correlation number between atoms [94, 37]. We assume A and M_S stay constant with Ga^+ irradiation, since they are typically bulk parameters and the interactions in the sample investigated in this chapter are dominated by the interfaces (see chapter 2). Values for K_{eff} are also required to extract D. However, since K_{eff} changes with Ga^+ irradiation (see chapter 3), we need values at each Ga^+ dose to accurately extract D from the model. From domain size measurements alone, we cannot extract values for K_{eff}, but we can estimate the changes in K_{eff} by comparison with results from ref [60], where the effective anisotropy of Pt/Co/Pt wires as a function of Ga^+ dose was studied. By calculating the percentage change in K_{eff} and applying this to the measured K_{eff} for our stack at zero dose (0.11 MJ/m^3 [37]) we can estimate the changes in K_{eff} for our stack. By combining all these parameters with the measured domain size at each Ga^+ dose, we can extract the changes in D due to Ga^+ irradiation.

Using the above described assumptions, we can form a hypothesis for the changes in domain size due to Ga^+ irradiation. From the assumptions that M_S and A are invariant, we expect the demagnetization energy to stay constant. From the expectation that D changes similarly to the surface anisotropy K_s (both are dependent on interface roughness), we expect the domain wall energy to decrease. A decreasing domain wall energy should result in a decrease in domain size, according to the model by Draaisma and de Jonge. This is caused by a relatively stronger demagnetization energy, which favors the creation of more domains and thus results in a lower domain size.

Qualitative changes in the domain structure as a result of Ga^+ irradiation can be seen from SEMPA measurements, shown in figures 6.1a and b. In figure 6.1a a domain structure is shown before irradiation, and in figure 6.1b after irradiation with $5 \cdot 10^{12}$ Ga^+ ions/cm^2. The SEMPA measurements are binarized to isolate the m_z (OOP) component. Up- and down domains are represented by white and black colors respectively. It is clearly visible that the size of the magnetic domains has decreased due to Ga^+ irradiation. This is as expected for decreasing domain wall energy, as described above. We can quantify the average domain size (indicated with a red bar in figure 6.1a) with a 2D fast Fourier transform, as described in detail in ref [95]. In figure 6.1c, the result of this domain size analysis for multiple Ga^+ doses is shown. Data points have been gathered until the magnetization turned in-plane due to negative K_{eff} (see chapter 2). From figure 6.1c, a decrease in domain size can be observed for increasing Ga^+ dose. This is conform our expectations and qualitative observations from figures 6.1a and b. The domain size seems to stabilize at a constant value for larger Ga^+ doses, which is in accordance with results observed in other techniques (e.g. magnetic force microscopy) [87]. The exact reason for this stabilization is not yet known. It is most likely due to a balance between the exchange interaction and demagnetization energy in the domain energy terms (see chapter 2), since these are assumed to be invariant with Ga^+ irradiation.

Now that we have measured the domain size as a function of Ga^+ dose, we can use the model by Draaisma and de Jonge to calculate changes in D. This is shown in figure 6.1d, where D is plotted as a function of Ga^+ dose. From figure 6.1d, we indeed see a decrease in D as a function of Ga^+ irradiation. This is as expected, due to the increased interface roughness induced by Ga^+ irradiation. As mentioned, increasing interface roughness is expected to lower D. Hence the fact that D decreases with increasing Ga^+ irradiation is as expected.

However, we expected to see a similar exponential decrease in D as the surface anisotropy K_s, as previously investigated [60], which is not the case for the measurements in figure 6.1d. The decrease in D seems to be linear in figure 6.1d. This suggests that K_{eff} and D are not the only

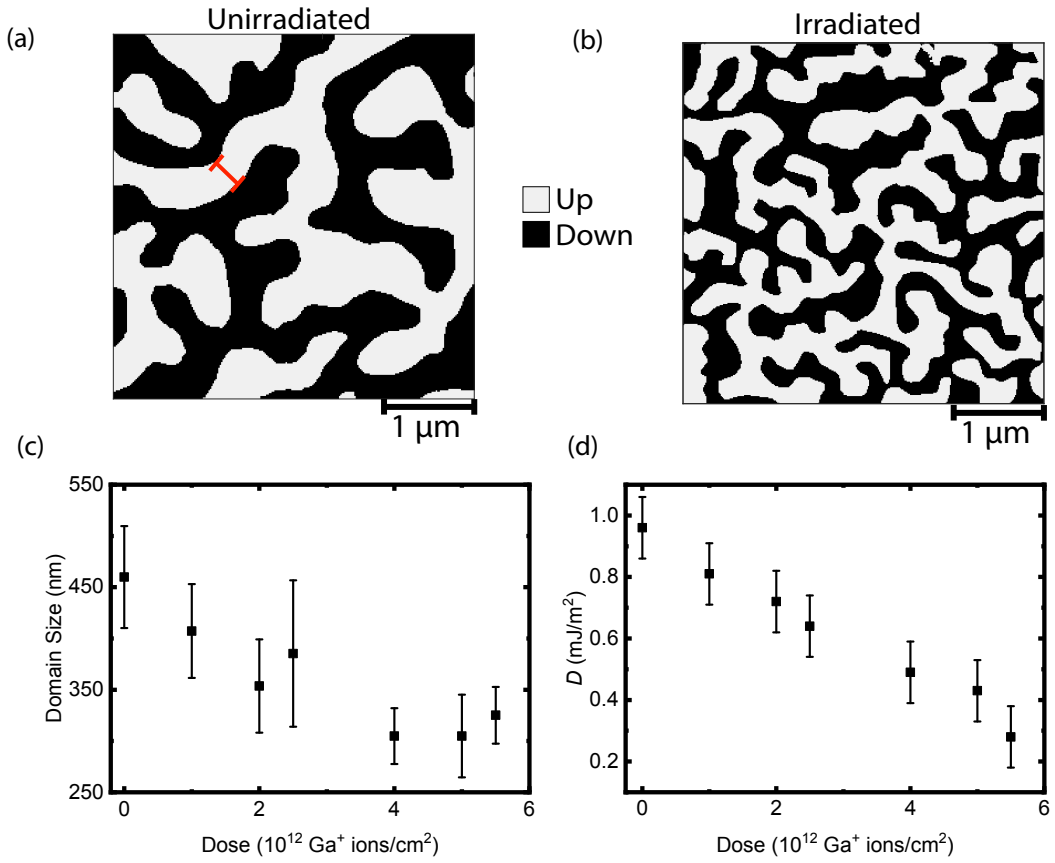

Figure 6.1: (a)-(b) Domain structures (m_z data) from SEMPA after a binarization step . Up- and down domains are represented by white and black colors respectively. (a) un-irradiated and (b) irradiated with $5 \cdot 10^{12}$ Ga$^+$ ions/cm^2. In (a) the red bar denotes the average domain size. (c) Domain size as a function of Ga$^+$ dose from SEMPA measurements. (d) Resulting values of the DMI as a function of Ga$^+$ dose from the model by ref [47].

parameters that change with Ga$^+$ irradiation. Changes in M_S due to Ga$^+$ irradiation have already been observed in single repeat W/CoFeB/MgO systems [96], and from the results in figure 6.1d we expect that M_S also changes in the multi-layered samples used in this chapter. Hence our initial assumption that M_S stays constant with Ga$^+$ irradiation may be incorrect. Incorporating changes in M_S in this model might result in changes in D which are similar to K_s, due to its impact on the demagnetizing field and effective anisotropy (see chapter 2). Furthermore, the observed decrease in D is roughly 71%, or 40% when changes in M_S are taken into account [87], which is significantly larger than expected, since K_s changes by roughly 15% [60]. Note that the change in K_s is extracted from a Pt/Co/Pt composition, which is likely one of the reasons why the decrease in D is not quantitatively similar to the expected decreased K_s [60]. The measured value of D at zero dose is also almost twice as large as the observed D in literature [37], which is likely caused by the same factors as described above. To extract more accurate values of D, individual measurements of K_{eff} at each Ga$^+$ dose have to be done. Furthermore, using more accurate models for the domain size (e.g. by ref [93], which takes into account the magnetic charges in the domain wall) can result in more realistic changes in D.

Several methods of measuring K_{eff} exist (such as SQUID-VSM, see chapter 3), but most of them are done ex-situ, and hence are incompatible with our samples. However, with SEMPA we are able to measure domain walls, whose width depends only on K_{eff} and A, the latter of which is

assumed to stay constant. This property can be used to extract K_{eff} values at different Ga^+ doses. In the next section, we will discuss the measurements on the domain wall width. We will also introduce a new experiment based on the domain wall chirality, which opens up another possibility for measuring D.

6.2 Effect of Ga^+ irradiation on domain walls

6.2.1 Domain wall width

As mentioned in section 6.1, the calculations for changes in D due to Ga^+ irradiation can be improved by directly measuring K_{eff}. In this section, we will calculate K_{eff} at each Ga^+ dose from the changes in domain wall width due to Ga^+ irradiation. As mentioned in chapter 2, the domain wall width is inversely proportional to $\sqrt{K_{\text{eff}}}$. Since Ga^+ irradiation decreases K_{eff}, we expect the domain size to increase with Ga^+ irradiation. Note that the investigations in this section are mainly preliminary, since no dedicated domain wall width experiments are performed.

An example of the domain size analysis method we used is shown in figure 6.2. We can extract the domain wall profile directly from the SEMPA data (see chapter 3), which is shown in figure 6.2a. Here, the SEMPA data from the m_{x} detector is shown, which shows the magnetic contrast in the horizontal x-direction (left-right). The arrow color codes the contrast to the magnetization direction. Similarly, data is also analyzed from the m_{y} (up-down) detector, but that is not shown here. The analysed domain wall is shown in the black box, which is enlarged in figure 6.2b. Due to the primary electron beam being much larger than the domain walls, the measured domain wall profile is enlarged. Hence we have to act with caution when extracting the domain wall width Δ_{top} from figure 6.1b. We can fit the domain wall profile with a Gaussian, which we can use to extract the actual domain wall width Δ_{top}, following refs [37] and [97]. The Gaussian fit is shown in figure 6.2c, where the black dots indicate the magnetic contrast in the analyzed area and the Gaussian fit is shown in red.

We can then extract K_{eff} from the expression by ref [98]; $K_{\text{eff}} = 4\frac{A}{\Delta_{\text{top}}^2}$, where A is the exchange stiffness. The measured values for Δ_{top} and K_{eff} can be seen in figure 6.2d. On the left axis and in red, Δ_{top} is shown, on the right axis and in blue, the corresponding K_{eff} values are shown as a function of Ga^+ irradiation. Measured values for Δ_{top} are in the range for what is expected from the expression in ref [98][1], however figure 6.2d shows very large fluctuations in both Δ_{top} and K_{eff} as a function of Ga^+ dose. This is not as expected for decreasing K_{eff} as a function of Ga^+ dose. Hence, this data is inconclusive and not suitable for use in models to extract D.

Several factors can be the cause of this inconclusive data. The first is electron shot noise (or Poisson noise) [99], which is present in every SEMPA scan. By averaging the data over more scans[2], this can be reduced. A second factor is the lack of pixels in the domain wall profile, which is caused by scanning at a relatively large scale. Hence by scanning in a smaller region, the domain size can be extracted more accurately. Both these factors have to do with data optimization. The data quality can also be improved by optimizing the analysis method. As shown in figure 6.2, the data is analyzed from one detector at a time (either m_{x} or m_{y}). By analyzing the data from the composite images, this issue can be solved.

Concluding, in this section we looked at the changes in domain wall width with Ga^+ irradiation to extract K_{eff} values, which could be used for the calculations in section 6.1. No clear trend in K_{eff} was observed, hence these preliminary investigations are inconclusive. However, it is expected that realistic values of K_{eff} can be extracted by performing dedicated domain wall width studies.

[1] When using values for A and K_{eff} from ref [37].
[2] The data in figure 6.2a was averaged over 5 scans.

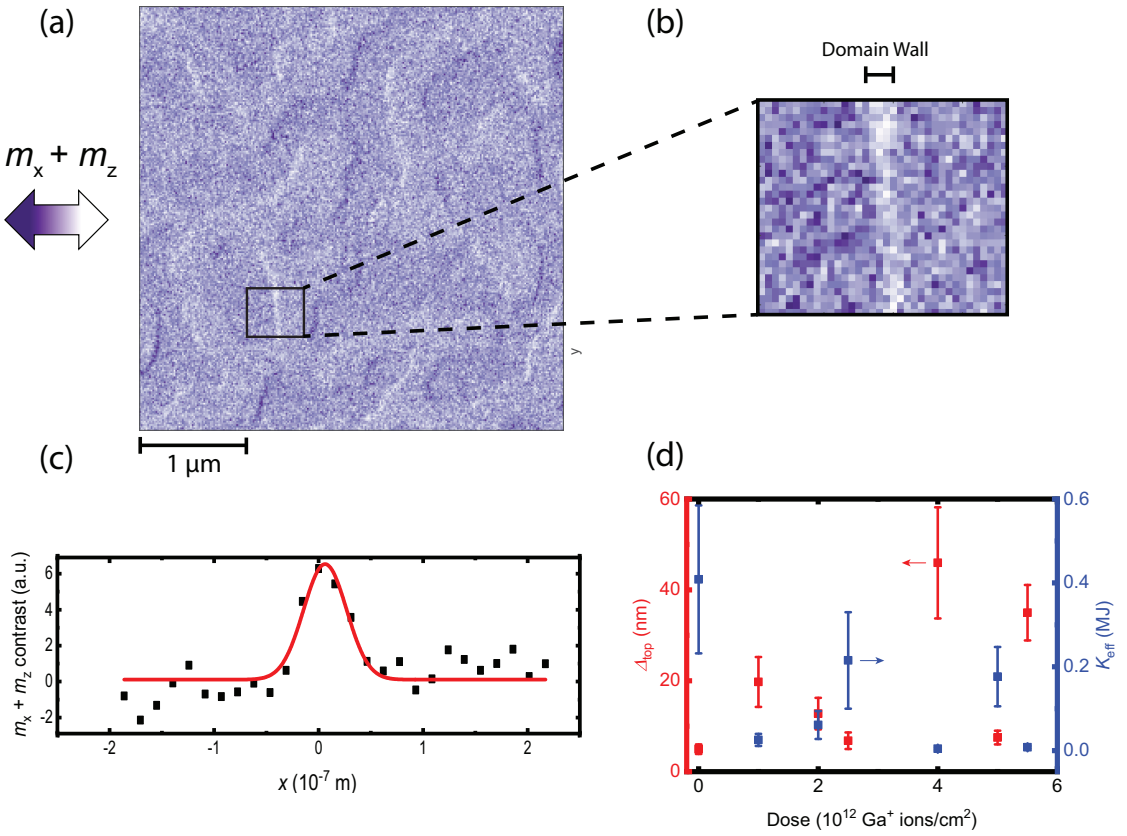

Figure 6.2: (a) m_x (+ OOP, m_z) data from which the domain walls are analysed. The analysed area is indicated with a black box. (b) Zoom of the analysed area, indicated in (a). (c) Gaussian fit of the domain wall profile in (b), from which the domain size is extracted. (d) Domain wall width (red, left axis) and resulting effective anisotropy (blue, right axis) as a function of Ga^+ irradiation.

The domain wall width is not the only property of domain walls that can be used to extract changes in magnetic parameters due to Ga^+ irradiation. In the next section, we will propose a new experiment based on the domain wall chirality to extract changes in D.

6.2.2 Domain wall chirality

As described in section 2.2.2, the chirality of a domain wall (direction of the magnetization in the domain wall) is dependent on the interplay between the dipolar energy and DMI. We can make use of this competition to investigate the changes in D due to Ga^+ irradiation. As mentioned in chapter 2 and section 6.1, we expect the DMI to decrease similar to K_s with Ga^+ irradiation due to interface roughening. Decreasing the DMI can result in a shift in domain wall chirality from counter-clockwise (CCW) to Bloch (B) to clockwise (CW) (see chapter 2).

Since we expect both the DMI and anisotropy to change with Ga^+ irradiation, we can use the model by ref [48] (see section 2.2.2) to calculate the domain wall chirality for a range of K_s and D values for the Ta(4)/Pt(2)/[Pt(1)/CoB(0.7)/Ir(1)]$_{x6}$/Pt(1)/CoB(0.8) stack investigated in this thesis. This gives us an idea how significant D and K_s are for inducing a chirality shift. The results of this calculation are shown in figure 6.3, where the domain wall chirality is color coded with the color bar on the right. α denotes the domain wall angle, as defined in chapter 3. The corresponding

chirality is shown in brackets. Values for K_s and D before irradiation are indicated with black lines and a black circle labelled (a) [37]. Here we have assumed that A and M_S are invariant with Ga^+ irradiation, and hence are kept constant at 12 pJ/m and 0.49 MA/m, respectively. Note that this assumption might be invalid, as mentioned in section 6.1 and ref [96]. In single layered systems a decrease in M_S for increasing Ga^+ dose was observed, which can also be the case for our multi-layered samples. Regarding A research is currently ongoing on how it changes with ion irradiation [87]. The expected position after Ga^+ irradiation is indicated with a black dot labelled (b). In figure 6.3 can be seen that, to change the chirality from CCW to CW, a much smaller decrease in D is required compared to K_s. Hence, although K_s does have an effect on the chirality, changing D is suspected to be the dominant factor if a chirality shift is observed.

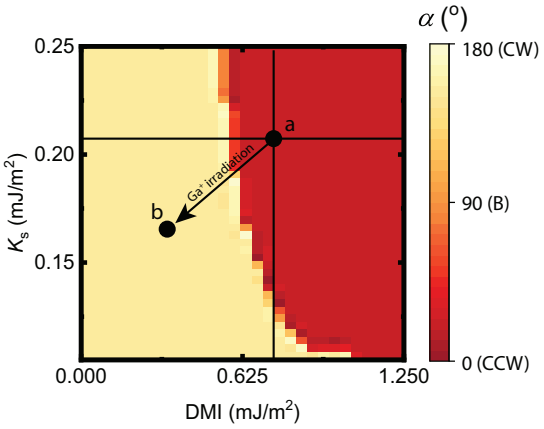

Figure 6.3: Theoretical calculation of the domain wall chirality using the model by ref [48] for a Ta(4)/Pt(2)/[Pt(1)/CoB(0.7)/Ir(1)]$_{x6}$/Pt(1)/CoB(0.8) multi-layered stack for different values of the DMI and the surface anisotropy K_s. The colorbar denotes the domain wall angle α. K_s and D values before irradiation are indicated with black lines and a black circle (a). The black circle at (b) indicates the prediction of the parameters after irradiation (qualitatively).

To verify our hypothesis for a chirality shift, we compare an un-irradiated area of the sample with an area of the sample which has been irradiated with $5 \cdot 10^{12}$ Ga^+ ions/cm^2. The results of these experiments are shown in figures 6.4. In figure 6.4a, the composite images (see chapter 3) are shown, with the un-irradiated and irradiated on the left and right sides respectively. Up- and down magnetization is represented in white and black respectively, while the in-plane magnetization in the domain walls is color coded according to the color wheel. Here, we see a significant decrease in average domain size, as already discussed in section 6.1.

To measure the domain wall chirality, we measure the domain wall angle α, defined as the angle between the magnetization m and the domain wall normal n and shown in the inset on the left in figure 6.4b. By counting α for all pixels in the domain walls, we can construct a histogram. The value of α with the most counts in the histogram tells us the chirality of the domain walls, with $\alpha = 0°$, $\pm 90°$ and $180°$ corresponding to counterclockwise (CCW), Bloch (B) and clockwise (CW) chirality respectively (see chapter 2). In figure 6.4b, the histograms for the domain wall angle α for all pixels in the domain walls are shown. We also fitted the histograms with a Gaussian to calculate the peak location, full width at half maximum (FWHM) and vertical offset. The values for the peak location, FWHM and offsets of the Gaussian fits are found in table 6.1.

The histograms in figure 6.4 and fit data in table 6.1 show that there is no shift in domain wall chirality after irradiation, since they are both peaked around $\alpha = 0$ (CCW). What is evident is the increased FWHM of the histogram after irradiation. This indicates a larger spread in domain wall angles, assuming similar experimental conditions between measurements (see supplementary of ref [37]). The vertical offset of the Gaussian fit is also larger. This means there are more counts

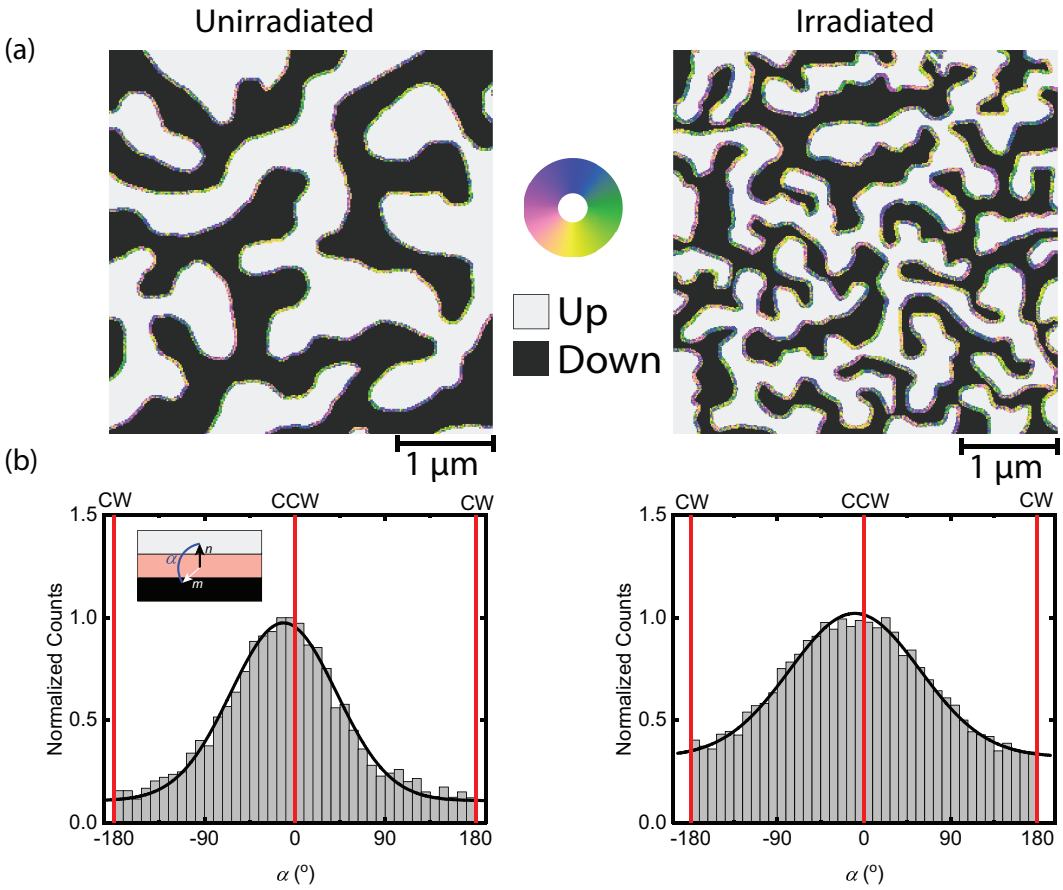

Figure 6.4: (a) Composite SEMPA images and (b) domain wall angle histograms for an un-irradiated area (left) and an area irradiated with $5 \cdot 10^{12}$ Ga^+ ions/cm^2 (right). The inset in the histogram of the un-irradiated area contains the definition of α. A Gaussian fit is shown over the histograms.

at all angles, which further reinforces this argument.

An increase in domain wall angle spread can indicate a move towards Bloch walls, especially due to the increased amount of counts at $\alpha = \pm 90°$. However for a full Bloch profile a clear peak around these values should be observed. Hence, it is more likely that the ion irradiation created more interface roughness, which results in a larger variation in K_{eff} and D values across the sample (as evident by the increase in FWHM in figure 6.4 for the irradiated area).

Furthermore, we expected to see a change from CCW to CW domain wall chirality due to an expected decrease of the DMI. However no changes were seen, which indicates that D and K_s are not the only parameters which are changing. Hence, we expect that our initial assumption that A and M_S are invariant with Ga^+ irradiation is indeed incorrect, as also discussed in section 6.1. Since M_S and A play a role in the model calculations, we have to their changes in the calculations to see how the chirality profile changes. From this, a more accurate prediction can be made as to how the chirality of a domain wall is expected to change with Ga^+ irradiation. From this new prediction, the changes in D due to ion irradiation can be better understood.

Concluding, in this section we proposed a new experiment, where changes in domain wall chirality due to Ga^+ irradiation can be used to extract changes in D. No changes in domain wall chirality were observed, even though it was expected from the calculations. A better understanding of how

Table 6.1: Fit values for the Gaussian fits in figure 6.4.

Ga^+ dose (10^{12} Ga^+ ions/cm^2)	Peak Location (°)	FWHM (°)	Vertical offset
0	-4 ± 5	33 ± 1	0.11 ± 0.01
5	-3 ± 5	43 ± 3	0.32 ± 0.04

the domain wall chirality changes with Ga^+ irradiation can be gained by incorporating changes in M_S into the model, which was most likely wrongly assumed to be invariant with Ga^+ irradiation. An increased spread in the domain wall angle α was seen, which can indicated increased variations in magnetic parameters across the sample due to more disordered interfaces.

6.3 Summary

In this chapter, we attempted to elucidate how magnetic parameters change due to Ga^+ irradiation. We did this to gain insights into the role Ga^+ irradiation plays in the stabilization of skyrmions at zero magnetic field for SEMPA imaging, both for inducing confinement (see chapter 4) and for tuning magnetic properties to aid stabilization.

In section 6.1 we looked at the changes in domain structure due to Ga^+ irradiation. A decrease in domain size was observed, which is consistent with expectations for decreasing K_{eff}. We used a model to extract changes in D due to Ga^+ irradiation and we found that the decrease in D was significantly larger than expected and not similar to changes in K_s. This gave us indications that it was wrongly assumed that M_S and is invariant under Ga^+ irradiation. To more accurately represent changes in D values for K_{eff} were also needed, which for the calculations we estimated by comparison to ref [60]. The calculations for D can be improved by measuring K_{eff} directly, which we proposed to do via domain walls.

In section 6.2 we looked at the changes in domain walls with Ga^+ irradiation. We investigated the domain wall width to extract K_{eff} values, which could be used in the calculations in section 6.1. No clear trend in K_{eff} was observed however, hence these investigations turned out to be inconclusive. To solve this, dedicated domain wall width measurements and analysis techniques are required.

We also proposed a new experiment, where we investigated changes in domain wall chirality with Ga^+ irradiation to extract changes in D. No shift in domain wall chirality was observed, hence changes in D could not be extracted. A better understanding of how the domain wall chirality changes with Ga^+ irradiation can be gained by incorporating changes in M_S into the model. An increase in domain wall angle spread was observed, which can indicate increased variations in magnetic parameters across the sample, due to more disordered interfaces after Ga^+ irradiation.

Chapter 7

Conclusions and Outlook

In this thesis, we proposed the use of a focused ion beam (FIB) to enhance skyrmion stabilization at zero magnetic field. We did this to move towards imaging the internal structure of skyrmions with SEMPA. With the FIB, we are able to modify magnetic parameters or create skyrmion confining structures, which could both enhance skyrmion stabilization at zero magnetic field. The effects of confined geometries on skyrmion stabilization was investigated with micro-magnetic simulations, while we used SEMPA to investigate the effects of Ga^+ ion irradiation on the magnetic domain- and domain wall structures. Since the FIB had never been used for quantitative Ga^+ ion irradiation experiments, a calibration method was required in the form of domain wall injection experiments. The conclusions of these simulations and experiments are summarized and some suggestions for future research will be given in this chapter.

Skyrmions in nanodots

In the micromagnetic simulations of chapter 4, we identified a simulation strategy analogous to ref [26], which we can use to investigate skyrmion stability in confined geometries. We investigated the magnetic phase in the geometries for a range of DMI values and geometry diameters. By comparison with experimentally obtained values of the DMI, we found that skyrmion stabilization at zero field can be achieved. Furthermore, we found that the simulations for skyrmion nucleation were unable to properly simulate the skyrmion nucleation. We were able to find good agreement in the low- and high magnetic field limits, so we mainly attributed the inability to simulate meta-stable skyrmions to fluctuations in D and K_{eff}, which were not taken account. Hence, to improve the method for simulating skyrmion nucleation, these fluctuations have to be included in the simulations. Furthermore, we mentioned that the simulated nanodots represented physical confinement with no surrounding magnetic material, instead of confinement in an area with PMA surrounded by an area with in-plane magnetization. Although we do not expect the results to change significantly, this needs to be taken into account for an optimal representation of future experiments. Other than creating confined structures, we also proposed the use of a FIB to tune magnetic properties, to potentially aid skyrmion stabilization. We investigated this in chapter 6 experimentally, however it would be interesting to know how changes in M_{S}, K_{eff}, A and D impact the skyrmion stability phase diagrams.

We can make a prediction on the effect of Ga^+ irradiation on the skyrmion stability phase diagrams, using realistic changes in M_{S}, K_{eff}, A and D as a function of Ga^+ irradiation. As discussed, the results in the phase diagrams are mainly dependent on the interplay between the domain wall energy, demagnetization energy and confinement. Hence we will use these energies to discuss the effects of Ga^+ irradiation. The domain wall energy is dependent on $\sqrt{A}$, $\sqrt{K_{\text{eff}}}$ and D. We already

know that K_{eff} and D decrease with Ga^+, where K_{eff} is expected to decrease more strongly than D due to additional changes in M_S, as we expect from chapter 6. Since we expect A to stay constant, we expect that the domain wall energy decreases after Ga^+ irradiation. A decrease in domain wall energy effectively lowers the critical D_{crit} value for spin spiral formation, and hence it is expected that the areas for skyrmion stabilization and chiral labyrinth state formation shift to lower D values. The demagnetization energy is fully dependent on M_S, which we assumed to stay constant with Ga^+ irradiation in chapter 6. However, we have seen indications that M_S does change with Ga^+ irradiation, meaning that the demagnetization energy also decreases with Ga^+ irradiation. A lower demagnetization energy effectively increases the domain size, hence we expect that the skyrmion and chiral labyrinth states shift to larger dot diameters. Combining these effects, we expect a total shift of the skyrmion stability pocket to lower D and larger dot diameter values after Ga^+ irradiation.

FIB calibration: domain wall injection

In chapter 5, we used domain wall injection experiments to calibrate the Ga^+ dose of the in-situ FIB. We also established that our methods for calculating the Ga^+ dose of the in-situ FIB was in good agreement with the calculations for a pre-calibrated FIB. This indicates that we can accurately predict the Ga^+ dose of the in-situ FIB, especially at lower doses, which is the region of interest for magnetic manipulation. Furthermore, we also found that we can easily tune the resolution in the in-situ FIB, although this was not quantified and should be investigated further. Accurate control over the size of the Ga^+ beam is required for creating sharp boundaries between irradiated areas and to be able to create small enough structures such that skyrmions can be confined, as discussed in chapter 4. The resolution can be quantified from the width of the anisotropy barrier, which is directly linked to the slope of the depinning dominant regime for the domain wall injection measurements.

Tuning magnetic parameters with Ga^+ irradiation

In chapter 6, we used the results from chapter 5 to investigate the changes in magnetic parameters from Ga^+ irradiation. From models for the domain size, we extracted a decrease in D as a function of Ga^+ irradiation. Qualitatively this agreed with our expectation that D does decrease with Ga^+ irradiation, however we did not observe the expected decreasing exponential scaling of D, similar to K_s. We expect that incorporating changes in M_S and A, which were assumed to be invariant with Ga^+ irradiation, into the calculations can help towards obtaining the expected scaling. In an effort to improve this calculation with specific K_{eff} values at each dose, we investigated the domain wall width as a function of Ga^+ dose. Although we could not measure specific K_{eff} values from these measurements, we established the need for dedicated domain wall width measurements to solve the issues we encountered. We also proposed a new experiment, based on the domain wall chirality, to extract changes in D due to Ga^+ irradiation. Although no shift in domain wall chirality was observed and thus changes in D could not be extracted, we identified clues that the variations in magnetic parameters increased due to Ga^+ irradiation.

Relating these conclusions to the goal of achieving SEMPA imaging of skyrmions, we can conclude we made progress in the right direction. We verified a micro-magnetic procedure to predict skyrmion stability, which remains to be verified experimentally, and we enabled the use of the in-situ FIB for quantitative Ga^+ dose experiments, an example of which we performed to extract changes in magnetic parameters. This experiment was mostly preliminary and hence the most improvements can be made in this area. These results show the first ever combined FIB and SEMPA measurements on multi-layered samples, which reveal that we can manipulate the magnetic properties on the tenths of naometer length scale. Further investigation is needed to understand all aspects of the conducted measurements. Mainly underlying assumptions on the

changes of micromagnetic parameters need to be eliminated, which is subject of ongoing research.

7.1 Disentangling magnetic parameters

In this thesis we established a need for dedicated measurements of M_S as a function of Ga^+ irradiation to accurately describe the experiments in chapter 6. In chapter 3 we mentioned that the typical method for measuring M_S is SQUID-VSM. However SQUID-VSM can only measure the magnetization of the entire sample, which is not useful when we want to measure the magnetization on small irradiated areas. In this section, we will propose several methods for extracting changes in M_S after Ga^+ ion irradiation at micrometer length scales.

Focused laser MOKE

The focused laser magneto-optical Kerr effect (MOKE, see chapter 3) can be used to obtain hysteresis loops at the micrometer scale, by focusing a laser spot on a small area and measuring the rotation of the polarization of the laser as a function of an applied field. Hence, this technique can be used to extract the changes in M_S from the maxima and minima of the hysteresis loops [28, 87]. MOKE does not directly measure the magnetization. Hence, a SQUID-VSM measurement is always required to link the MOKE measurements to the magnetization. Focused laser MOKE is incompatible with the typical samples used in SEMPA measurements, since it is performed ex-situ, requiring a capping layer. However it can be used to qualitatively estimate changes in M_S in very small areas, which is not possible with a standalone SQUID-VSM. Furthermore, no extra processing steps are required to perform this technique.

μ-SQUID

Rather than using a standalone SQUID-VSM, the Josephson junctions that are used in SQUID-VSM measurements can also be grown directly onto the sample by electron beam lithography (EBL), as shown by ref [100]. This technique is called micro-SQUID, or μ-SQUID, and can be used to measure both K_{eff} and M_S at micrometer length scales. Contrary to focused laser MOKE, this technique directly measures the magnetization and can thus be used to quantitatively describe changes in M_S in very small areas. However, due to the use of EBL, which is performed ex-situ and requires extra processing steps, this technique is incompatible with the typical samples used for SEMPA.

Scanning probe magnetometry

Other than directly depositing Josephson junctions on top of the sample, they can directly be attached to a scanning probe microscopy probe. This is a technique called scanning probe magnetometry [101]. Similar to atomic force microscopy, the probe is scanned across the surface, measuring the magnetization using the SQUID-VSM method with a spatial resolution of roughly 1 μm [101]. This technique can be performed in-situ, although not at our labs, and does not require extra processing steps, making it compatible with the typical SEMPA samples.

Bibliography

[1] A. Hylick, R. Sohan, A. Rice, and B. Jones, "An analysis of hard drive energy consumption," in *2008 IEEE International Symposium on Modeling, Analysis and Simulation of Computers and Telecommunication Systems*, pp. 1–10, IEEE, 2008.

[2] V. Kasavajhala, "Solid state drive vs. hard disk drive price and performance study," *Proc. Dell Tech. White Paper*, pp. 8–9, 2011.

[3] S. S. Parkin, M. Hayashi, and L. Thomas, "Magnetic domain-wall racetrack memory," *Science*, vol. 320, no. 5873, pp. 190–194, 2008.

[4] M. Hayashi, L. Thomas, R. Moriya, C. Rettner, and S. S. Parkin, "Current-controlled magnetic domain-wall nanowire shift register," *Science*, vol. 320, no. 5873, pp. 209–211, 2008.

[5] A. Brataas, A. D. Kent, and H. Ohno, "Current-induced torques in magnetic materials," *Nature materials*, vol. 11, no. 5, p. 372, 2012.

[6] D. Ravelosona, D. Lacour, J. A. Katine, B. D. Terris, and C. Chappert, "Nanometer scale observation of high efficiency thermally assisted current-driven domain wall depinning," *Phys. Rev. Lett.*, vol. 95, p. 117203, Sep 2005.

[7] G. Tatara and H. Kohno, "Theory of current-driven domain wall motion: Spin transfer versus momentum transfer," *Phys. Rev. Lett.*, vol. 92, p. 086601, Feb 2004.

[8] A. Fert, N. Reyren, and V. Cros, "Magnetic skyrmions: Advances in physics and potential applications," *Nature Reviews Materials*, vol. 2, 2017.

[9] W. Legrand, D. Maccariello, N. Reyren, K. Garcia, C. Moutafis, C. Moreau-Luchaire, S. Collin, K. Bouzehouane, V. Cros, and A. Fert, "Room-temperature current-induced generation and motion of sub-100 nm skyrmions," *Nano letters*, vol. 17, no. 4, pp. 2703–2712, 2017.

[10] F. Jonietz, S. Mühlbauer, C. Pfleiderer, A. Neubauer, W. Münzer, A. Bauer, T. Adams, R. Georgii, P. Böni, R. A. Duine, *et al.*, "Spin transfer torques in MnSi at ultralow current densities," *Science*, vol. 330, no. 6011, pp. 1648–1651, 2010.

[11] N. Nagaosa and Y. Tokura, "Topological properties and dynamics of magnetic skyrmions," *Nature Nanotechnology*, vol. 8, no. 12, p. 899, 2013.

[12] A. Fert, V. Cros, and J. Sampaio, "Skyrmions on the track," *Nature nanotechnology*, vol. 8, no. 3, p. 152, 2013.

[13] S. Zhang, A. A. Baker, S. Komineas, and T. Hesjedal, "Topological computation based on direct magnetic logic communication," *Scientific reports*, vol. 5, p. 15773, 2015.

[14] X. Zhang, G. Zhao, H. Fangohr, J. P. Liu, W. Xia, J. Xia, and F. Morvan, "Skyrmion-skyrmion and skyrmion-edge repulsions in skyrmion-based racetrack memory," *Scientific reports*, vol. 5, p. 7643, 2015.

[15] I. Kézsmárki, S. Bordács, P. Milde, E. Neuber, L. Eng, J. White, H. M. Rønnow, C. Dewhurst, M. Mochizuki, K. Yanai, *et al.*, "Néel-type skyrmion lattice with confined orientation in the polar magnetic semiconductor GaV_4S_8," *Nature materials*, vol. 14, no. 11, p. 1116, 2015.

[16] C. Moreau-Luchaire, C. Moutafis, N. Reyren, J. Sampaio, C. Vaz, N. Van Horne, K. Bouzehouane, K. Garcia, C. Deranlot, P. Warnicke, *et al.*, "Additive interfacial chiral interaction in multilayers for stabilization of small individual skyrmions at room temperature," *Nature nanotechnology*, vol. 11, no. 5, p. 444, 2016.

[17] S. Woo, K. Litzius, B. Krüger, M.-Y. Im, L. Caretta, K. Richter, M. Mann, A. Krone, R. M. Reeve, M. Weigand, *et al.*, "Observation of room-temperature magnetic skyrmions and their current-driven dynamics in ultrathin metallic ferromagnets," *Nature materials*, vol. 15, no. 5, p. 501, 2016.

[18] A. Soumyanarayanan, M. Raju, A. G. Oyarce, A. K. Tan, M.-Y. Im, A. P. Petrović, P. Ho, K. Khoo, M. Tran, C. Gan, *et al.*, "Tunable room-temperature magnetic skyrmions in Ir/Fe/-Co/Pt multilayers," *Nature materials*, vol. 16, no. 9, p. 898, 2017.

[19] I. Lemesh and G. S. Beach, "Twisted domain walls and skyrmions in perpendicularly magnetized multilayers," *Physical Review B*, vol. 98, no. 10, p. 104402, 2018.

[20] J. Unguris, "Scanning electron microscopy with polarization analysis (SEMPA) and its applications," in *Experimental methods in the physical sciences*, vol. 36, pp. 167–XVI, Elsevier, 2001.

[21] H. Oepen and H. Hopster, "SEMPA studies of thin films, structures, and exchange coupled layers," in *Magnetic Microscopy of Nanostructures*, pp. 137–167, Springer, 2005.

[22] R. Frömter, S. Hankemeier, H. P. Oepen, and J. Kirschner, "Optimizing a low-energy electron diffraction spin-polarization analyzer for imaging of magnetic surface structures," *Review of Scientific Instruments*, vol. 82, no. 3, p. 033704, 2011.

[23] S. Rohart and A. Thiaville, "Skyrmion confinement in ultrathin film nanostructures in the presence of Dzyaloshinskii-Moriya interaction," *Physical Review B*, vol. 88, no. 18, p. 184422, 2013.

[24] J. Sampaio, V. Cros, S. Rohart, A. Thiaville, and A. Fert, "Nucleation, stability and current-induced motion of isolated magnetic skyrmions in nanostructures," *Nature nanotechnology*, vol. 8, no. 11, p. 839, 2013.

[25] R. Tomasello, K. Guslienko, M. Ricci, A. Giordano, J. Barker, M. Carpentieri, O. Chubykalo-Fesenko, and G. Finocchio, "Origin of temperature and field dependence of magnetic skyrmion size in ultrathin nanodots," *Physical Review B*, vol. 97, no. 6, p. 060402, 2018.

[26] P. Ho, A. K. Tan, S. Goolaup, A. G. Oyarce, M. Raju, L. Huang, A. Soumyanarayanan, and C. Panagopoulos, "Geometrically Tailored Skyrmions at Zero Magnetic Field in Multilayered Nanostructures," *Physical Review Applied*, vol. 11, no. 2, p. 024064, 2019.

[27] A. P. van Liempt, "Tuning Magnetic Multilayers for Skyrmion Nucleation," Master's thesis, Eindhoven University of Technology, 2019.

[28] J. M. Coey, *Magnetism and magnetic materials*. Cambridge University Press, 2010.

[29] H. Ibach and H. Luth, *Solid state physics: an introduction to principles of materials science*. Cambridge University Press, 4 ed., 2010.

[30] C. F. Schippers, "Measuring a peak shift in propagating spin-wave spectroscopy," Master's thesis, Eindhoven University of Technology, 2018.

[31] M. Johnson, P. Bloemen, F. Den Broeder, and J. De Vries, "Magnetic anisotropy in metallic multilayers," *Reports on Progress in Physics*, vol. 59, no. 11, p. 1409, 1996.

[32] D. Weller, Y. Wu, J. Stöhr, M. Samant, B. Hermsmeier, and C. Chappert, "Orbital magnetic moments of Co in multilayers with perpendicular magnetic anisotropy," *Physical review B*, vol. 49, no. 18, p. 12888, 1994.

[33] T. Devolder, "Light ion irradiation of Co/Pt systems: Structural origin of the decrease in magnetic anisotropy," *Physical Review B*, vol. 62, no. 9, p. 5794, 2000.

[34] J. D. Jackson, *Classical Electrodynamics*. Wiley, 2 ed., 1975.

[35] P. Carcia, "Perpendicular magnetic anisotropy in Pd/Co and Pt/Co thin-film layered structures," *Journal of applied physics*, vol. 63, no. 10, pp. 5066–5073, 1988.

[36] P. Shepley, A. Rushforth, M. Wang, G. Burnell, and T. Moore, "Modification of perpendicular magnetic anisotropy and domain wall velocity in Pt/Co/Pt by voltage-induced strain," *Scientific reports*, vol. 5, p. 7921, 2015.

[37] J. Lucassen, M. J. Meijer, O. Kurnosikov, H. J. M. Swagten, B. Koopmans, R. Lavrijsen, F. Kloodt-Twesten, R. Frömter, and R. A. Duine, "Tuning magnetic chirality by dipolar interactions," *Phys. Rev. Lett.*, vol. 123, p. 157201, 2019.

[38] I. Dzyaloshinksii, "A thermodynamic theory of weak ferromagnetism of antiferromagnetics," *J. Phys. Chem. Solids*, vol. 4, pp. 241–255, 1958.

[39] T. Moryia, "Anisotropic superexchange interaction and weak ferromagnetism.," *Phys. Rev.*, vol. 120, pp. 91–98, 1960.

[40] H. T. Nembach, J. M. Shaw, M. Weiler, E. Jué, and T. J. Silva, "Linear relation between Heisenberg exchange and interfacial Dzyaloshinskii–Moriya interaction in metal films," *Nature Physics*, vol. 11, no. 10, p. 825, 2015.

[41] A. Thiaville, S. Rohart, É. Jué, V. Cros, and A. Fert, "Dynamics of Dzyaloshinskii domain walls in ultrathin magnetic films," *EPL (Europhysics Letters)*, vol. 100, no. 5, p. 57002, 2012.

[42] J. H. Franken, M. Herps, H. J. Swagten, and B. Koopmans, "Tunable chiral spin texture in magnetic domain-walls," *Scientific reports*, vol. 4, p. 5248, 2014.

[43] M. Heide, G. Bihlmayer, and S. Blügel, "Dzyaloshinskii-Moriya interaction accounting for the orientation of magnetic domains in ultrathin films: Fe/W (110)," *Physical Review B*, vol. 78, no. 14, p. 140403, 2008.

[44] A. Hubert and R. Schäfer, "Magnetic Domains," *Berlin, Heidelberg, New York, pgs*, vol. 255, 1998.

[45] A. Mougin, M. Cormier, J. Adam, P. Metaxas, and J. Ferré, "Domain wall mobility, stability and walker breakdown in magnetic nanowires," *EPL (Europhysics Letters)*, vol. 78, no. 5, p. 57007, 2007.

[46] S. Middelhoek, "Domain walls in thin Ni–Fe films," *Journal of Applied Physics*, vol. 34, no. 4, pp. 1054–1059, 1963.

[47] H. Draaisma and W. De Jonge, "Magnetization curves of Pd/Co multilayers with perpendicular anisotropy," *Journal of applied physics*, vol. 62, no. 8, pp. 3318–3322, 1987.

[48] W. Legrand, J.-Y. Chauleau, D. Maccariello, N. Reyren, S. Collin, K. Bouzehouane, N. Jaouen, V. Cros, and A. Fert, "Hybrid chiral domain walls and skyrmions in magnetic multilayers," *Science advances*, vol. 4, no. 7, p. eaat0415, 2018.

[49] M. J. Meijer. Personal Communication.

[50] A. Malozemoff, J. Slonczewski, and R. Wolfe, "Applied Solid State Science," in *Magnetic Domain Walls in Bubble Materials*, pp. 77–83, Academic Press, 1979.

[51] W. Legrand, N. Ronceray, N. Reyren, D. Maccariello, V. Cros, and A. Fert, "Modeling the shape of axisymmetric skyrmions in magnetic multilayers," *Physical Review Applied*, vol. 10, no. 6, p. 064042, 2018.

[52] Y. Dovzhenko, F. Casola, S. Schlotter, T. Zhou, F. Büttner, R. Walsworth, G. Beach, and A. Yacoby, "Magnetostatic twists in room-temperature skyrmions explored by nitrogen-vacancy center spin texture reconstruction," *Nature communications*, vol. 9, no. 1, p. 2712, 2018.

[53] K. Fallon, S. McVitie, W. Legrand, F. Ajejas, D. Maccariello, S. Collin, V. Cros, and N. Reyren, "Quantitative imaging of hybrid chiral spin textures in magnetic multilayer systems by Lorentz microscopy," *arXiv preprint arXiv:1901.03652*, 2019.

[54] A. Hrabec, J. Sampaio, M. Belmeguenai, I. Gross, R. Weil, S. M. Chérif, A. Stashkevich, V. Jacques, A. Thiaville, and S. Rohart, "Current-induced skyrmion generation and dynamics in symmetric bilayers," *Nature communications*, vol. 8, p. 15765, 2017.

[55] T. Lichtenberg, "Stabilizing skyrmion bubbles in patterned nanostructures," Master's thesis, Eindhoven University of Technology, 2018.

[56] H. Du, R. Che, L. Kong, X. Zhao, C. Jin, C. Wang, J. Yang, W. Ning, R. Li, C. Jin, *et al.*, "Edge-mediated skyrmion chain and its collective dynamics in a confined geometry," *Nature communications*, vol. 6, p. 8504, 2015.

[57] F. C. Ummelen, T. Lichtenberg, H. J. M. Swagten, and B. Koopmans, "Controlling skyrmion bubble confinement by dipolar interactions," *Applied Physics Letters*, vol. 115, no. 10, p. 102402, 2019.

[58] A. van den Brink, *New directions for magnetic memory : alternative switching mechanisms for magnetic random-access memory.* PhD thesis, Eindhoven University of Technology, 9 2016.

[59] M. J. Meijer In Preparation.

[60] J. H. Franken, M. Hoeijmakers, R. Lavrijsen, and H. J. M. Swagten, "Domain-wall pinning by local control of anisotropy in Pt/Co/Pt strips," *Journal of Physics: Condensed Matter*, vol. 24, no. 2, p. 024216, 2011.

[61] J. H. Franken, *Domain walls shift gears - Novel ways to control magnetic domain-wall motion.* PhD Thesis, Eindhoven University of Technology, 2014.

[62] C. A. Volkert and A. M. Minor, "Focused Ion Beam Micromachining," *MRS Bulletin*, vol. 32, no. May 2007, pp. 389–399, 2007.

[63] J. Mayer, L. A. Giannuzzi, T. Kamino, and J. Michael, "TEM sample preparation and FIB-induced damage," *MRS bulletin*, vol. 32, no. 5, pp. 400–407, 2007.

[64] M. D. Uchic, L. Holzer, B. J. Inkson, E. L. Principe, and P. Munroe, "Three-dimensional microstructural characterization using focused ion beam tomography," *MRS Bulletin*, vol. 32, no. 5, pp. 408–416, 2007.

[65] R. M. Langford, P. M. Nellen, J. Gierak, and Y. Fu, "Focused ion beam micro-and nanoengineering," *MRS bulletin*, vol. 32, no. 5, pp. 417–423, 2007.

[66] W. J. MoberlyChan, D. P. Adams, M. J. Aziz, G. Hobler, and T. Schenkel, "Fundamentals of focused ion beam nanostructural processing: Below, at, and above the surface," *MRS bulletin*, vol. 32, no. 5, pp. 424–432, 2007.

[67] Orsay Physics, Manual Canion 31U UHV FIB.

[68] T. Aign, P. Meyer, S. Lemerle, J. Jamet, J. Ferré, V. Mathet, C. Chappert, J. Gierak, C. Vieu, F. Rousseaux, *et al.*, "Magnetization reversal in arrays of perpendicularly magnetized ultrathin dots coupled by dipolar interaction," *Physical review letters*, vol. 81, no. 25, p. 5656, 1998.

[69] C. Vieu, J. Gierak, H. Launois, T. Aign, P. Meyer, J. Jamet, J. Ferré, C. Chappert, V. Mathet, and H. Bernas, "High resolution magnetic patterning using focused ion beam irradiation," *Microelectronic engineering*, vol. 53, no. 1-4, pp. 191–194, 2000.

[70] R. Hyndman, P. Warin, J. Gierak, J. Ferré, J. Chapman, J. Jamet, V. Mathet, and C. Chappert, "Modification of Co/Pt multilayers by gallium irradiationPart 1: The effect on structural and magnetic properties," *Journal of Applied Physics*, vol. 90, no. 8, pp. 3843–3849, 2001.

[71] D. Kumar and A. Adeyeye, "Techniques in micromagnetic simulation and analysis," *Journal of Physics D: Applied Physics*, vol. 50, no. 34, p. 343001, 2017.

[72] J. Leliaert and J. Mulkers, "Tomorrows micromagnetic simulations," *Journal of Applied Physics*, vol. 125, no. 18, p. 180901, 2019.

[73] A. Vansteenkiste, J. Leliaert, M. Dvornik, M. Helsen, F. Garcia-Sanchez, and B. Van Waeyenberge, "The design and verification of Mumax3," *AIP Advances*, vol. 4, no. 10, p. 107133, 2014.

[74] J. Mulkers, B. Van Waeyenberge, and M. V. Milošević, "Effects of spatially-engineered Dzyaloshinskii-Moriya interaction in ferromagnetic films," *Physical Review B*, vol. 95, no. 14, p. 144401, 2017.

[75] W. Rave, K. Ramstöck, and A. Hubert, "Corners and nucleation in micromagnetics," *Journal of magnetism and magnetic materials*, vol. 183, no. 3, pp. 329–333, 1998.

[76] M. Peeters, "Domain Wall Depinning using the precession-torque," Master's thesis, Eindhoven University of Technology, 2016.

[77] Z. Qiu and S. D. Bader, "Surface magneto-optic Kerr effect," *Review of Scientific Instruments*, vol. 71, no. 3, pp. 1243–1255, 2000.

[78] J. Lucassen, F. Kloodt-Twesten, R. Frömter, H. P. Oepen, R. A. Duine, H. J. Swagten, B. Koopmans, and R. Lavrijsen, "Scanning electron microscopy with polarization analysis for multilayered chiral spin textures," *Applied Physics Letters*, vol. 111, no. 13, p. 132403, 2017.

[79] M. J. Meijer, J. Lucassen, F. Kloodt-Twesten, R. Frömter, O. Kurnosikov, R. A. Duine, H. J. Swagten, B. Koopmans, and R. Lavrijsen, "Magnetic chirality controlled by the interlayer exchange interaction," *arXiv preprint arXiv:1909.08909*, 2019.

[80] J. Lucassen, *Exploring chiral magnetism with spin waves and domain walls.* PhD thesis in preparation, Eindhoven University of Technology.

[81] J. Clarke and A. I. Braginski, *The SQUID handbook*, vol. 1. Wiley Online Library, 2004.

[82] B. de Loos, "Magnetic Force Microscopy: Application to Magnetic Nanostructures," Master's thesis, Eindhoven University of Technology, 2006.

[83] M. Baćani, M. A. Marioni, J. Schwenk, and H. J. Hug, "How to measure the local Dzyaloshinskii-Moriya Interaction in skyrmion thin-Film Multilayers," *Scientific reports*, vol. 9, no. 1, p. 3114, 2019.

[84] J. Franken, H. Swagten, and B. Koopmans, "Shift registers based on magnetic domain wall ratchets with perpendicular anisotropy," *Nature nanotechnology*, vol. 7, no. 8, p. 499, 2012.

[85] L. H. Diez, M. Voto, A. Casiraghi, M. Belmeguenai, Y. Roussigné, G. Durin, A. Lamperti, R. Mantovan, V. Sluka, V. Jeudy, *et al.*, "Enhancement of the Dzyaloshinskii-Moriya interaction and domain wall velocity through interface intermixing in Ta/CoFeB/MgO," *Physical Review B*, vol. 99, no. 5, p. 054431, 2019.

[86] A. Casiraghi, A. Magni, L. H. Diez, J. Langer, B. Ocker, M. Pasquale, D. Ravelosona, and G. Durin, "Bloch-to-Néel domain wall transition evinced through morphology of magnetic bubble expansion in Ta/CoFeB/MgO layers," *arXiv preprint arXiv:1907.03708*, 2019.

[87] M. C. H. de Jong, "Working title: the effect of Ga^+ ion irradiation on the stabilization and current driven nucleation of skyrmions." Preliminary MSc. thesis results.

[88] R. Lavrijsen, D. Hartmann, A. van den Brink, Y. Yin, B. Barcones, R. Duine, M. Verheijen, H. Swagten, and B. Koopmans, "Asymmetric magnetic bubble expansion under in-plane field in Pt/Co/Pt: Effect of interface engineering," *Physical Review B*, vol. 91, no. 10, p. 104414, 2015.

[89] E. Fatuzzo, "Theoretical considerations on the switching transient in ferroelectrics," *Physical review*, vol. 127, no. 6, p. 1999, 1962.

[90] S. Pizzini, J. Vogel, S. Rohart, L. D. Buda-Prejbeanu, E. Jué, O. Boulle, I. M. Miron, C. K. Safeer, S. Auffret, G. Gaudin, and A. Thiaville, "Chirality-Induced Asymmetric Magnetic Nucleation in Pt/Co/AlO_x Ultrathin Microstructures," *Phys. Rev. Lett.*, vol. 113, p. 047203, Jul 2014.

[91] P. Lendecke, R. Eiselt, G. Meier, and U. Merkt, "Temperature dependence of domain-wall depinning fields in constricted Permalloy nanowires," *Journal of Applied Physics*, vol. 103, no. 7, p. 073909, 2008.

[92] X. Zhao, B. Zhang, N. Vernier, X. Zhang, M. Sall, T. Xing, L. H. Diez, C. Hepburn, L. Wang, G. Durin, *et al.*, "Enhancing domain wall velocity through interface intermixing in W-CoFeB-MgO films with perpendicular anisotropy," *Applied Physics Letters*, vol. 115, no. 12, p. 122404, 2019.

[93] I. Lemesh, F. Büttner, and G. S. Beach, "Accurate model of the stripe domain phase of perpendicularly magnetized multilayers," *Physical Review B*, vol. 95, no. 17, p. 174423, 2017.

[94] C. Eyrich, A. Zamani, W. Huttema, M. Arora, D. Harrison, F. Rashidi, D. Broun, B. Heinrich, O. Mryasov, M. Ahlberg, *et al.*, "Effects of substitution on the exchange stiffness and magnetization of Co films," *Physical Review B*, vol. 90, no. 23, p. 235408, 2014.

[95] J. W. van der Jagt, "MFM on Skyrmionic Systems," Bachelor's thesis, Eindhoven University of Technology, 2017.

[96] L. H. Diez, F. García-Sánchez, J.-P. Adam, T. Devolder, S. Eimer, M. El Hadri, A. Lamperti, R. Mantovan, B. Ocker, and D. Ravelosona, "Controlling magnetic domain wall motion in the creep regime in He^+-irradiated CoFeB/MgO films with perpendicular anisotropy," *Applied Physics Letters*, vol. 107, no. 3, p. 032401, 2015.

[97] E. C. Corredor, S. Kuhrau, F. Kloodt-Twesten, R. Frömter, and H. P. Oepen, "SEMPA investigation of the Dzyaloshinskii-Moriya interaction in the single, ideally grown Co/Pt (111) interface," *Physical Review B*, vol. 96, no. 6, p. 060410, 2017.

[98] B. Lilley, "LXXI. Energies and widths of domain boundaries in ferromagnetics," *The London, Edinburgh, and Dublin Philosophical Magazine and Journal of Science*, vol. 41, no. 319, pp. 792–813, 1950.

[99] W. Schottky, "Über spontane Stromschwankungen in verschiedenen Elektrizitätsleitern," *Annalen der physik*, vol. 362, no. 23, pp. 541–567, 1918.

[100] A. Ronzani, M. Baillergeau, C. Altimiras, and F. Giazotto, "Micro-superconducting quantum interference devices based on V/Cu/V Josephson nanojunctions," *Applied Physics Letters*, vol. 103, no. 5, p. 052603, 2013.

[101] Y. Shibata, S. Nomura, H. Kashiwaya, S. Kashiwaya, R. Ishiguro, and H. Takayanagi, "Imaging of current density distributions with a Nb weak-link scanning nano-SQUID microscope," *Scientific reports*, vol. 5, p. 15097, 2015.

Appendix A

Simulation supplementary information

In this appendix, we provide supplementary data for the simulations conducted in chapter 4. We will first discuss the simulation recipes for skyrmion stabilization and nucleation. Afterwards, we will investigate the effect of different initial conditions on the outcome of the simulations, such that we can select the initial condition which best describes the experimental results. Finally, we will compare simulation results with those conducted by ref [26], to verify that we are using a correct simulation strategy.

A.1 Simulation recipe

For both the skyrmion stabilization and nucleation simulations performed in chapter 4, we use the following simulation properties:

- Cell sizes of 2×2 nm^2 in the x - y plane, and 0.6 nm in the z-direction, corresponding to the thickness of the magnetic layer, are used. These values are smaller than the typical exchange length $l_s = \sqrt{\frac{A}{\mu_0 M_S^2}} \approx 3$ nm.
- Cylindrical geometry, with height equal to the amount of magnetic layers. For single layers, this is equal to 1. For multi-layers, the total amount of magnetic layers is equal to the amount of repeats, with an approximately 2 nm spacer layer injected between each magnetic layer. The thickness of the spacer layers is taken closest to nearest multiple of the magnetic layer thickness.
- Values for M_S, A and K_{eff} are set at 1.0 MA/m^3, 10 pJ/m and 0.35 MJ/m^3, respectively [27]. We set an easy anisotropy axis in the z-direction.

Skyrmion stabilization

For the skyrmion stability simulations, we initialized a Néel skyrmion with a charge of 1 and core polarization of -1. We let the magnetization relax with the relax command. This process is repeated for DMI values of 0.5 to 5.0 mJ/m^2, with steps of 0.5 mJ/m^2, and dot diameter values of 100 to 700 nm, with steps of 100 nm.

Skyrmion nucleation

For the skyrmion nucleation simulations, a random magnetization state is relaxed with the relax command. Next, a magnetic field is applied in the z-direction, from 0 mT to B_{max}, in steps of 0.1 B_{max}, with B_{max} the magnetic field where the magnetization in the nanodot is saturated. Between each field step, the magnetization is relaxed with the relax command. This process is repeated for dot diameters between values of 100 and 700 nm, with steps of 100 nm. We set the DMI at values of 1.0 mJ/m^2, 1.7 mJ/m^2 and 2.38 mJ/m^2 in different simulation sets. For the different sets, B_{max} was set at 100 mT, 200 mT and 400 mT respectively.

A.2 Nanodot phase for various initial conditions

In this section, we investigate the effect of different initial conditions on the outcome of the stabilization simulations, such that we can accurately describe experiments. We used the same simulation recipe as mentioned in section A.1. We simulated a single repeat layer of Ir(1)/Fe(0.4)Co(0.6)/Pt, with magnetic parameters from ref [26]. We expect that the conclusions drawn for a single Ir/-FeCo/Pt layer are also applicable to the multi-layered Ir/Co/Pt stack used in the simulations of chapter 4.

Simulations with 4 different initial conditions have been performed, and the results are shown in figure A.1; (a) a Néel skyrmion, (b) random magnetization, (c) a two domain structure and (d) uniform magnetization. The colorbar on the right shows the color coding for the different phases, as defined in section 4.1. It is immediately apparent that the phase diagrams for the different initial conditions are very different from each other, which means that selecting the correct initial conditions is vital for an accurate representation of an experimental situation. A Néel skyrmion investigates the stability of a skyrmion that is already present in the sample. This initial condition is also used by ref [26]. Random magnetization will result in a ground state that is found from a very high energy state. Conversely, a two-domain state is already close to the experimentally observed ground state [59]. Last, the uniform magnetization tests the stability of the UM state. For the investigations into skyrmion stabilization by confinement, the most suitable initial condition is the Néel skyrmion. For the investigations into skyrmion nucleation in confined structures, results for the random magnetization initial condition resemble experimentally observed states at zero field the most [59], since the multi-domain state is present at low DMI. Although the two-domain initial condition is very close to the ground state, observed symmetry effects in the ground state will play a role in determining the final state, hence starting from a high energy random state will more accurately represent the experimentally found final states. From the results of uniform magnetization, we can conclude that the UM state is very stable and not suitable for the investigations into skyrmion nucleation.

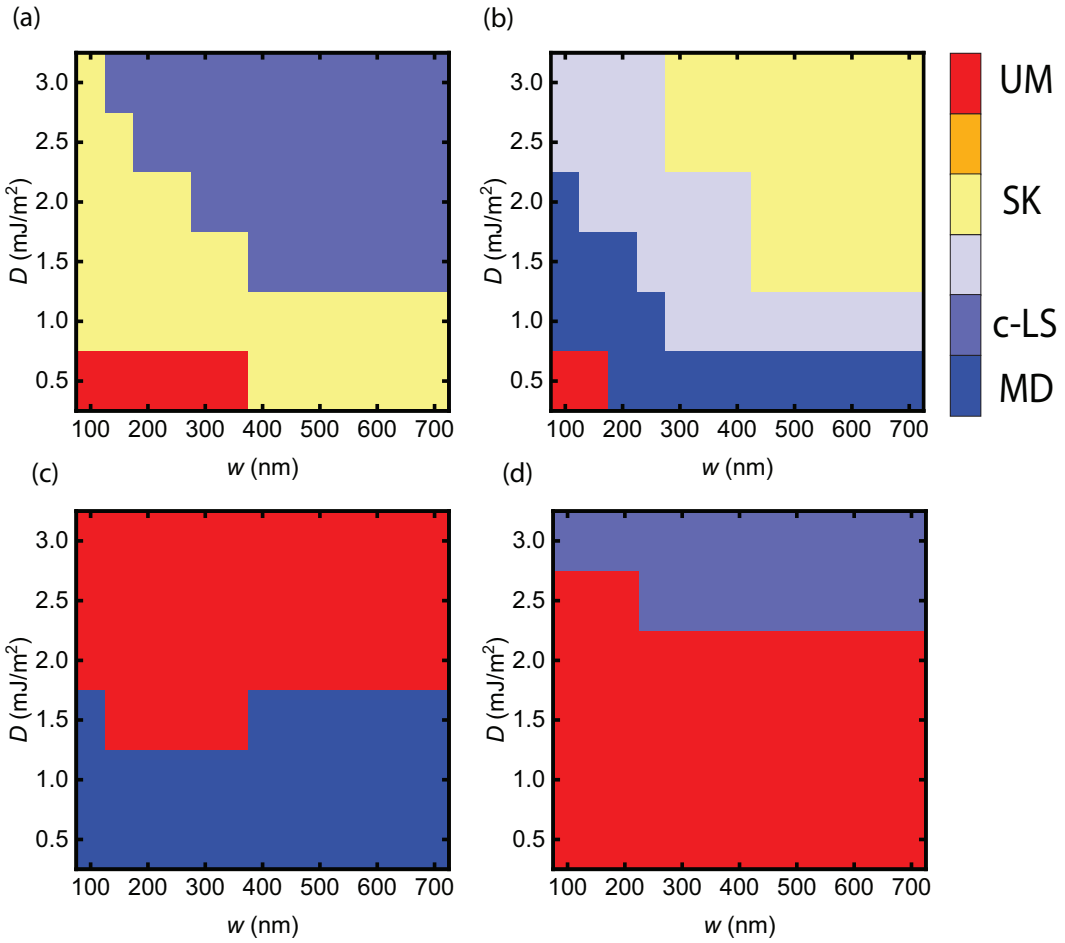

Figure A.1: Simulated zero-field phase diagrams of the $[Ir(1)/Fe(0.4)Co(0.6)/Pt(1)]_{20}$ nanodots with different initial conditions. (a) Néel skyrmion, (b) random magnetization, (c) two domain structure and (d) uniform magnetization.

A.3 Verification of the simulation strategy

In this section, we attempt to recreate the results of Ho *et al.* [26] to verify our simulation strategy for skyrmion stabilization in nanodots. We will use the strategy as defined in section A.1 for skyrmion stabilization in $[Ir(1)/Fe(0.4)/Co(0.6)/Pt(1)]_{20}$ nanodots, with material parameters as described in ref [26].

The resulting phase diagrams for skyrmion stabilization are shown in figure A.2, where figure A.2a shows the results by ref [26] and figure A.2b shows the results using our strategy. Comparison between figures A.2a and b shows that the three phases exist around roughly the same parameter values. Despite some discrepancies between the two figures, which are mainly present due to the manual identification of the simulated results, this gives us confidence that we can use this method for determining the stability of skyrmions in confined structures.

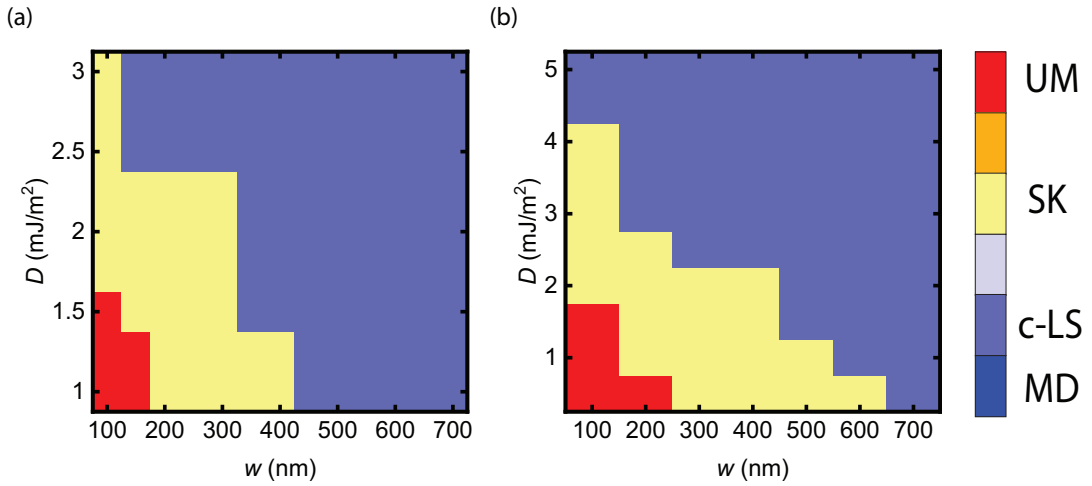

Figure A.2: Simulated zero-field phase diagram of the $[Ir(1)/Fe(0.4)/Co(0.6)/Pt(1)]_{20}$ nanodots. (a) Simulations by ref [26]. (b) Simulations performed with our strategy.

Appendix B

Nanowire fabrication recipe

In this appendix, we discuss the recipe to create the wires used in the domain wall injection measurements in chapter 5. The working principles of EBL have already been discussed in section 3.1.3.

1. We clean the sample substrate, Si with a thermally oxidized SiO_2 layer of 100 nm, with aceton and isopropanol respectively in an ultrasonic bath.
2. Two layers of PMMA resist are spin coated on the sample substrate. The bottom layer consists of PMMA 450K, whereas the top layer consists of PMMA 950K. Each layer is spinned for 60 seconds at 3000 RPM. After each spinning step, the sample is heated on a hot-plate at 150 °C for 1 minute.
3. The wire patterns are created with EBL using the electron beam at 30 keV in a FEI Nova dualbeam system.
4. After EBL, the sample is developed in a 1:3 MIBK:IPA mixture for 80 seconds, and IPA for 1 minute, and subsequently dried with N_2.
5. The sample is covered in a Ta(4)/Pt(4)/Co(0.6)/Pt(4) stack by DC sputtering, with an Ar plasma at roughly 10^{-2} mbar. The system pressure is roughly 10^{-9} mbar.
6. Lift-off is subsequently performed in several acetone baths to remove the remaining resist. The sample is then cleaned in IPA.

Appendix C

In-situ FIB dose calculation

In this appendix, we describe two calculations for the Ga^+ dose of the in-situ FIB. First, we calculate the dose in C/m^2 for specific sets of parameters in the patterning engine of the FIB. Second, we calculate the required pixel dwell time to achieve a desired dose.

Before we can start calculating the dose, it is useful to know the specifications of the patterning engine, which prevents the calculation of invalid parameters. The patterning engine has a maximum pixel density of 4000×4000 pixels, with a maximum frequency of 24 MHz. This maximum frequency results in scanning times in multiples of 42 ns, which is the minimum scanning time per pixel.

Based on the unit of each parameter, a function can be constructed to calculate the dose of the FIB in charge per unit area. We will make use of the following parameters; (i) the beam current I_b, which is the amount of charge that hits the sample each second (in Amperes); (ii) the field of view F, which inversely proportional to the magnification and denotes the scale of each image axis (in meters); (iii) the amount of pixels on each axis N_pixel and (iv) the irradiation time per pixel t_irr (in seconds). Experimentally, we determine I_b by deflecting the beam into a picoammeter, which is built into the FIB. N_pixel can be determined by drawing an area with a known size. N_pixel can then be read directly from the software. F and t_irr can be set manually in the software.

First, we need to find the amount of pixels in a certain area. This can be done by first finding the amount of pixels per unit length, by dividing N_pixel by F. By then squaring it, we find the amount of pixels per unit area. The amount of charge on each pixel is simply the beam current times the pixel dwell time. By multiplying the amount of charge per pixel with the amount of pixels per area, we find the amount of charge per unit area, which we call the base dose D_base in C/m^2. In the form of an equation, this looks like

$$D_\mathrm{base} = \left(\frac{N_\mathrm{pixel}}{F}\right)^2 \cdot I_\mathrm{b} \cdot t_\mathrm{irr}. \tag{C.1}$$

By multiplying with $\frac{1}{e} \cdot 10^{-6}$, where e is the elementary charge, the unit can be converted to ions/cm^2, as is used throughout this thesis.

Equation C.1 can be modified to isolate t_irr, which is the time to reach a desired dose D_des. We do this because it gives us greater control over the Ga^+ dose. In an equation, this looks like

$$t_\mathrm{irr} = \frac{D_\mathrm{des}}{I_\mathrm{b}} \left(\frac{N_\mathrm{pixel}}{F}\right)^2. \tag{C.2}$$

Now that we have calculated the irradiation time to achieve the desired dose, we can multiply t_{irr} with an array containing dose factors to calculate the scanning time required for larger doses. Due to the patterning engine constraint that t_{irr} is always a multiple of 42 ns, we round the irradiation times to the closest multiple of 42 ns. The array containing all the rounded scanning times can then be used in equation C.1 to calculate the corrected doses. The uncertainty in the dose is calculated with standard error propagation. The main contributions to the error lie in I_{b} and N_{pixel}. With this information, we have everything we need to irradiate structures accurately.